Instrumentation Development and Testing for the ALBATROS Low-Frequency Interferometer

Tristan Ménard

Department of Physics

McGill University, Montréal

December, 2021

A thesis submitted to McGill University in partial fulfillment of the requirements of the degree of

Master of Science

Abstract

The cosmic dark ages was an early period in the universe's history beginning after recombination and lasting until the birth of the first stars. The 21-cm emission from neutral hydrogen in this era provides a valuable tracer with which to probe the state and evolution of the early universe. Due to cosmic expansion, 21-cm emission from the early universe is redshifted to radio frequencies, with the cosmic dark ages corresponding to frequencies below approximately 30 MHz. Ionospheric interference, radio-frequency interference (RFI) from human activity, and strong Galactic foreground emission make observations at such low frequencies exceptionally difficult to achieve. As such, the cosmic dark ages remain unexplored by observers to date despite holding a wealth of cosmological information. This thesis will discuss recent instrumentation developments for the Array of Long Baseline Antennas for Taking Radio Observations from the Sub-Antarctic/Seventy-ninth parallel (ALBATROS), an experiment aiming to map the radio sky below 30 MHz.

In its final state, ALBATROS will be an interferometric array composed of electrically small and autonomously operating antennas covering a frequency range from 1.2 to 125 MHz. Each antenna station will collect data independently and store it locally for later retrieval and correlation. Higher frequencies around 113 MHz are included for inter-station synchronization with aliased ORBCOMM signals. To avoid various sources of RFI, ALBATROS arrays will be deployed in extremely remote polar locations. Notably, ALBATROS antenna stations will be positioned with a maximum baseline length of 20 km, leading to an order of magnitude improvement in resolution compared to previous low-frequency observations. The detailed observational data from ALBATROS is expected to help identify the cosmological 21-cm signal from strong Galactic foregrounds at the lowest possible frequencies, thereby laying the groundwork for the first observations of the cosmic dark ages.

The experiment is currently in its early stages of development. Previous pathfinder experiments on Marion Island were successful and a team was deployed to the McGill Arctic Research Station in 2019 to assess RFI levels at the potential site. In this thesis, I will discuss recent developments to the ALBATROS instrument, including results from the first end-to-end system tests of the autonomous antenna station which was deployed at Uapishka Station in 2021 and features a methanol-solar hybrid power system, 128 terabytes of local data storage, as well as improved data acquisition hardware.

Résumé

Les âges sombres étaient une période dans le passé lointain de l'univers, commençant après la recombinaison et durant jusqu'à la naissance des premières étoiles. Le rayonnement à 21 cm par l'hydrogène neutre à cette époque est un traceur important pour sonder l'état et l'évolution de l'univers primitif. Dû à l'expansion de l'univers, le rayonnement à 21 cm dans l'univers juvénile est décalé vers le rouge et les âges sombres sont associés aux fréquences radios dessous approximativement 30 MHz. Les observations à ces basses fréquences sont exceptionnellement difficiles à réaliser en raison de l'interférence ionosphérique, des interférences radioélectriques (RFI) causées par l'activité humaine et des émissions galactiques fortes. Ainsi, les âges sombres demeurent inexplorés par les observateurs, alors qu'ils recèlent une véritable mine d'informations cosmologiques. Cette thèse discute des développements récents dans l'instrumentation du projet ALBATROS (Array of Long Baseline Antennas for Taking Radio Observations from the Sub-Antarctic/Seventy-ninth parallel), une expérience ayant pour but la production d'images interférométriques du ciel en ondes radios dessous 30 MHz.

Dans son état final, ALBATROS sera un réseau interférométrique composé d'antennes électriquement petites et fonctionnant de manière autonome entre 1,2 et 125 MHz. Chaque station d'antenne fera la collecte de données de manière indépendante et enregistrera les données localement. Les données seront récupérées manuellement et corrélées plus tard. Les fréquences plus élevées, autour de 113 MHz, sont incluses pour synchroniser toutes les stations avec les signaux aliasés d'ORBCOMM. Afin d'éviter les différentes sources de RFI, les stations d'antennes ALBATROS seront installées dans des endroits polaires hyper-isolés. Notamment, les stations d'antennes ALBATROS seront positionnées avec une longueur de ligne de base maximale de 20 km, ce qui permettra d'améliorer la résolution de l'expérience par un ordre de grandeur relativement aux observations à basse fréquence antécédentes. Les données observationelles détaillées obtenues par

ALBATROS aideront l'extraction du signal cosmologique à 21 cm des émissions galactiques fortes qui interviennent en avant-plan et agiront en tant que fondation pour les premières observations des âges sombres.

Actuellement, l'expérience est à son premier stade de développement. Des expériences éclaireuses à l'île Marion ont été réussi avec succès, puis une équipe a été envoyée à la station de recherche arctique McGill en 2019 pour évaluer les niveaux de RFI à ce site potentiel. Dans cette thèse, je discuterai des développements récents qui se rapportent à l'instrumentation d'ALBATROS, incluant les résultats des premiers tests de bout-en-bout de la station d'antenne autonome qui a été installée à la station Uapishka en 2021 et qui comporte un système d'alimentation hybride méthanol-solaire, un système d'enregistrement de données avec un volume de 128 TB, ainsi que du matériel amélioré pour le système de collecte de données.

Acknowledgements

There are many people that have contributed in one way or another to the work I have accomplished in these past couple years. A number of incredible people have encouraged me to reach for the stars and guided me along the way. First and foremost, I have to explicitly thank Cynthia Chiang, who has been the friendliest, most supportive supervisor I could ask for and who gave me the opportunity to take on this challenge. I had never heard of experimental cosmology until my first chat with Cynthia and I could not be happier to have my eyes opened to this wonderful field. I also have to thank Cynthia for helping me prepare and refine my thesis into a cohesive story that I am now proud to call my own. This work would also not have been possible without Eamon Egan, with whom I had countless conversations, exchanging ideas and questions, that helped push my research forward whenever a fresh perspective or new direction was needed. I learned something new in almost every one of our conversations. I would also like to thank Jon Sievers for helping me out with code-related problems at a few critical junctures as well as Gavin Noble for his great introduction to `rasp`. I am thankful to all my lab mates for helping me on a daily basis and to the rest of the team on the weekly ALBATROS/PRIZM/High-Z telecon call. Thank you to my friends at the Physics Department for creating such a supportive and fun community that helped keep me sane throughout this process. Some of the research work discussed in my thesis was accomplished at Uapishka Station and I would like to thank everyone at the station for their hospitality. I would also like to acknowledge that Uapishka is a constituent part of *Nitassinan*, the ancestral homeland of the Innu. Finally, and most importantly, I thank my family, especially my parents, and Kiera for all of your unconditional support over the years. I especially recognize the extra work all of you took on to help me focus on the task at hand over the final few weeks.

Table of Contents

Chapter 1

Introduction to 21-cm cosmology

In the beginning the Universe was created. This has made a lot of people very angry and been widely regarded as a bad move.

– Douglas Adams, *The Restaurant at the End of the Universe*

The universe is vast and intimidating. It's no wonder that we, as its citizens, have tried our best to make sense of it. Now, after thousands of years looking up to the cosmos, what do we know about the universe? Did it have a beginning, and if so, how did it start? How old is the universe? How big is it? One day, will the universe come to an end? There are so many questions one can throw into the vastness of the universe. For cosmologists, who study the universe's history and evolution, the most important question might just be: *how can we learn more?*

In 1929, Edwin Hubble made one of the most significant discoveries about the nature of the universe to date. Hubble observed that other galaxies are moving away from us. Moreover, the furthest galaxies are drifting away faster than closer ones, and a galaxy's observed velocity is proportional to its distance (Hubble, 1929). In this way, Hubble observed that the universe is expanding (Bahcall, 2015). Hubble's discovery also provided support to the Big Bang model, but the Big Bang still remained highly polarizing in the scientific community for decades afterwards. It was the discovery of the cosmic microwave background, an observation predicted by the Big Bang model, that finally brought widespread agreement on the issue (Ryden, 2016; Mo et al., 2010). The point of this story is that observations are the foundation upon which our cosmological knowledge of the universe is built.

Advancements in observational cosmology have led to amazing discoveries about the nature of the universe. Yet, despite all the recent progress in cosmology, our understanding of the universe is still incomplete. We are just starting to uncover the state of the universe at the time of the birth of the first stars, with surprising results so far to be sure (see Bowman et al., 2018). The observable period before the birth of the universe's first stars, aptly known as the cosmic "dark ages", remains entirely unexplored and serves as one of the final frontiers in observational cosmology. In this chapter, I will discuss how 21-cm cosmology experiments offer a promising avenue for gaining insight into early universe physics by detecting the redshifted 21-cm line from neutral hydrogen. Furthermore, this thesis will proceed to describe new progress in the development of the Array of Long Baseline Antennas for Taking Radio Observations from the Sub-Antarctic/Seventy-ninth parallel (ALBATROS), an interferometric array that will produce high-resolution images of the low-frequency radio sky with a view to pave the way towards future dark ages cosmology experiments.

1.1 Timeline of the universe's history

According to the Hot Big Bang (HBB) model, the current standard theory of cosmology, the universe was incredibly hot and dense in its first moments following the Big Bang. The physics of these very earliest moments are poorly understood as the conditions required to study such an intense environment exceed the capabilities of the world's most advanced laboratories. Nonetheless, it is thought that the universe underwent a very rapid period of exponential expansion called the inflationary epoch. The inflationary epoch would explain the high degree of homogeneity and flatness that is observed in the universe as well as its lack of magnetic monopoles (Brandenberger, 2011). As the universe went through this period of inflation, its contents quickly diluted and cooled by many orders of magnitude. Once the inflationary epoch ended, the universe continued to expand but in a decelerating manner.

The HBB model becomes clearer and more experimentally constrained about 10^{-10} s after the Big Bang, once the universe has cooled down to temperatures below 10^{16} K, or equivalently energies below 1 TeV. Then, when the temperature declined below 10^{12} K, elementary particles, such as bosons, leptons, mesons, and baryons, and their associated antiparticles began to emerge from the quark-gluon plasma of the very early universe (Roos, 2008). A few minutes after the Big Bang, the universe's temperature had reached 10^9 K (0.1 MeV) and created the appropriate conditions to enable the fusion of protons and neutrons into atomic nuclei. The primordial nuclei consisted mainly of hydrogen along with helium and trace amounts of lithium. The period encompassing the formation of primordial nuclei is called nucleosynthesis, and the relative abundances of each element after its completion are accurately predicted by HBB. This prediction marks one of the model's major successes (Baumann, 2012). Notably, the temperature of the universe was still too high to allow electrons to bind with nuclei. Thus, the universe became filled with a plasma of electrons and highly ionized nuclei.

Following primordial nucleosynthesis, photons, ionized nuclei, and free electrons interacted with one another in a number of ways. Importantly, protons (ionized hydrogen nuclei) and electrons began to recombine into neutral hydrogen atoms. Recombination proceeded via two-photon emission from electrons decaying to the *1s* ground state of hydrogen from the *2s* excited state. As the universe was optically thick, this reaction was critical because the two emitted photons did not possess enough energy to excite or ionize another hydrogen atom afterwards. Additionally, the cosmological redshift of photons to lower energies contributed towards an increased recombination rate (Peebles, 1968). Around 380,000 years after the Big Bang, the temperature of the universe had decreased to approximately 3000 K and very few photons possessed enough energy to ionize hydrogen, so nearly all nuclei and electrons recombined into neutral atoms. The epoch of recombination marked an important moment in the universe's history as it transitioned from an ionized state to a neutral one. At this time, Thomson scattering had become important, but the decreasing number density of free electrons due to the combined effects of recombination and cosmic expansion meant that these interactions became rare. Consequently, photons decoupled from matter, the universe became optically thin, and photons travelled freely through space for the first time (Mo et al., 2010). The surface of last scattering created by these photons is known as the cosmic microwave background (CMB). The prediction of the CMB's existence was another one of the HBB model's great successes. High precision measurements of the CMB spectrum show that it is an extremely isotropic and homogeneous blackbody with a temperature of 2.726 K (Fixsen, 2009).

Then, the universe entered the cosmic dark ages, a period during which there were very few sources of light. The only photons were those from the CMB and as well as 21-cm photons emitted by the spin-flip transition of neutral hydrogen. Throughout the cosmic dark ages, the neutral gas kept cooling adiabatically while overdense regions, believed to be seeded by quantum fluctuations during inflation, began to gravitationally collapse. These collapsing clouds became the birthplaces of the universe's first stars and galaxies, whose appearance heralded the beginning of a new epoch: cosmic dawn. The ultraviolet (UV) radiation from these stars ultimately ionized most of the gas during the epoch of reionization (Pritchard & Loeb, 2012). This time, however, the universe remained optically thin since cosmological expansion meant that the number density of free electrons was too small to sustain any kind of significant scattering rate (Mo et al., 2010). By the end of the epoch of reionization, the universe was almost entirely ionized so 21-cm photon emission became rare. Nevertheless, gravity continued to cause matter to collapse into the large-scale structures, such as stars, galaxies, and galaxy clusters, that we see today.

1.2 21-cm cosmology

Hubble's observation of the universe's expansion is one of the fundamental building blocks of any modern theory of cosmology. He discovered that distant galaxies recede away from us faster than nearer ones. The relationship between the distance to a galaxy and its recessional velocity is linear and is described by Hubble's law:

$$v = H_0 d, \tag{1.1}$$

where v is the recessional velocity, d is the proper distance and H_0 is the Hubble constant that relates these two quantities. The Hubble constant is an important cosmological parameter that gives the universe's current rate of expansion. However, there is tension surrounding the true value of the Hubble constant as different measurement methods have produced different values of H_0. Measurements of type Ia supernovae give $H_0 = 73.24 \pm 1.74\,\mathrm{km\,s^{-1}\,Mpc^{-1}}$ (Riess et al., 2016) while measurements of the CMB power spectrum give $H_0 = 67.66 \pm 0.42\,\mathrm{km\,s^{-1}\,Mpc^{-1}}$ (Planck Collaboration et al., 2020). These values disagree with one another by a notable margin.

Nonetheless, as the universe expands, the radiation travelling within it is redshifted to longer wavelengths and thus lower frequencies. The cosmological redshift parameter z corresponds to the fractional change in wavelength due to cosmic expansion. It can be expressed as

$$1+z=\frac{\nu_{\mathrm{em}}}{\nu_{\mathrm{obs}}}, \tag{1.2}$$

where ν_{em} is the frequency of the emitted radiation and ν_{obs} is the frequency of the radiation when it is observed. The larger the redshift, the longer the radiation has spent travelling through space. Therefore, cosmological redshift can be interpreted as a lookback time and increasing values of z correspond to earlier epochs in the universe's history.

1.2.1 Origin of the 21-cm signal

The decoupling of radiation and matter in the universe occurred at $z \approx 1090$ and allowed photons to travel freely through space for the first time (Hinshaw et al., 2009). Due to recombination, these decoupled CMB photons were released into a universe whose matter content consisted primarily of neutral hydrogen atoms. Furthermore, the slow influence of gravity meant that clouds of neutral hydrogen had not yet collapsed into stars and galaxies. As such, the universe transitioned into a new epoch: the cosmic dark ages, where there were no new sources of light except for radiation from the spin-flip transition of neutral atoms.

The spin-flip transition in neutral hydrogen results from the hyperfine splitting of its ground state into two energy levels. In turn, the hyperfine splitting of the hydrogen ground state can be explained by the energy difference between the triplet state, where the spins of the electron and proton are aligned, and the singlet state, where the spins are anti-aligned. The energy gap between these two hyperfine levels is $E_{10} = 5.9\,\mu\mathrm{eV}$, which is equivalent to a photon frequency of 1420 MHz or a wavelength of 21.1 cm (Pritchard & Loeb, 2012). The relative occupation of each hyperfine level is given by (Furlanetto et al., 2006)

$$\frac{n_1}{n_0}=\frac{g_1}{g_0}e^{-T_\star/T_S}, \tag{1.3}$$

where n_1/n_0 is the ratio of the number density of hydrogen atoms in the triplet state (denoted by a subscript 1) compared to the singlet state (denoted by a subscript 0). The spin degeneracy factor between the triplet and singlet state is $g_1/g_0 = 3$, while $T_\star \equiv E_{10}/k_B = 0.068\,\mathrm{K}$ is the equivalent temperature to the hyperfine energy gap. Finally, T_S is the spin temperature. The conclusion to draw from Equation 1.3 is that the relative occupation of the hyperfine levels is completely determined by the spin temperature. Consequently, the spin temperature directly affects the emission and absorption of 21-cm photons in a neutral hydrogen cloud.

As specified by Equation 1.2, the 21-cm line from the early universe is observed today as a signal covering a wide range of radio frequencies depending on the photon's age. Due to the abundance of neutral hydrogen, the 21-cm signal provides an important tracer for probing the state of the early universe and its evolution can be understood by the radiative transfer of background CMB photons through a gas of neutral hydrogen atoms. The basic radiative transfer equation for a specific intensity I_ν through an optical depth τ_ν is

$$\frac{dI_\nu}{d\tau_\nu} = S_\nu - I_\nu, \tag{1.4}$$

where S_ν is the source function defined by the ratio of the medium's emission and absorption coefficients. The solution to this differential equation for a uniform and homogeneous geometry has the form

$$I_\nu^{\mathrm{obs}} = I_\nu^{\mathrm{bg}} e^{-\tau_\nu} + S_\nu \left(1 - e^{-\tau_\nu}\right), \tag{1.5}$$

where I_ν^{obs} is the specific intensity observed after travelling through an optical depth τ_ν and I_ν^{bg} is the specific intensity of background radiation entering the medium. In the context of the early universe, the background radiation is the CMB blackbody spectrum with brightness temperature T_{CMB} and the medium is neutral hydrogen gas with spin temperature T_S. Now, due to the low frequencies in question, the specific intensities in Equation 1.5 can be easily re-written as brightness temperatures using the Rayleigh-Jeans limit.

$$I_\nu^{\mathrm{obs}} = \frac{2h\nu^2 T_b^{\mathrm{obs}}}{c^2}, \quad I_\nu^{\mathrm{bg}} = \frac{2h\nu^2 T_{\mathrm{CMB}}}{c^2}, \quad \text{and} \quad S_\nu = \frac{2h\nu^2 T_S}{c^2}, \tag{1.6}$$

where h is the Planck constant, c is the speed of light, and T_b^{obs} is the observed brightness temperature. Then, by making the appropriate substitutions, Equation 1.5 becomes

$$T_b^{\text{obs}} = T_{\text{CMB}} e^{-\tau_\nu} + T_S \left(1 - e^{-\tau_\nu}\right). \tag{1.7}$$

The observable 21-cm signal is measured relative to the CMB and must account for the expansion of the universe. Thus, the expected brightness temperature of the 21-cm signal δT_b as a function of redshift is

$$\delta T_b(z) = \frac{T_b^{\text{obs}} - T_{\text{CMB}}}{1+z} = \frac{(T_S - T_{\text{CMB}})(1 - e^{-\tau_\nu})}{1+z} \approx \frac{T_S - T_{\text{CMB}}}{1+z} \tau_\nu. \tag{1.8}$$

The final approximation in Equation 1.8 can be made since the optical depth is known to be small for all redshifts of interest. Additionally, Equation 1.8 highlights that the 21-cm signal may only be observed when the spin temperature deviates from the brightness temperature of the CMB (Pritchard & Loeb, 2012). When $T_S > T_{\text{CMB}}$ the signal appears in emission, but when $T_S < T_{\text{CMB}}$ the signal appears in absorption.

In terms of cosmological parameters, the 21-cm signal can be written as (Zaldarriaga et al., 2004):

$$\delta T_b(z) \approx 23\,\text{mK}\,(1+\delta) x_{\text{HI}} \left(1 - \frac{T_{\text{CMB}}}{T_S}\right) \left(\frac{\Omega_b h^2}{0.02}\right) \left[\left(\frac{0.15}{\Omega_m h^2}\right) \left(\frac{1+z}{10}\right)\right]^{1/2}, \tag{1.9}$$

where δ is the baryon overdensity, x_{HI} is the neutral fraction of hydrogen atoms, and Ω_b and Ω_m are, respectively, the critical density parameters for baryons and matter in the universe.

1.2.2 Evolution of the global signal

Spontaneous emission or absorption between the two hyperfine states is rare because the hyperfine transition has a very small Einstein coefficient of $A_{10} = 2.85 \times 10^{-15}\,\text{s}^{-1}$. Consequently, the timescale for a spin-flip transition to occur, which can be taken as the reciprocal of A_{10}, is approximately 11 million years. Since this is a relatively long timescale, there are a few faster mechanisms that govern the incidence of spin-flip transitions: interactions with the radio background, collisions between particles, as well as interactions with ultraviolet Lyα photons as described by the Wouthuysen-Field effect (Field, 1958). The manner by which these three processes cause spin-flip transitions and affect the spin temperature will be detailed in the following paragraphs.

Firstly, the simplest of these processes for exciting the hyperfine transition involves radiative interactions with background radio photons. Photons with the appropriate wavelength of 21 cm, which are mainly from the radio portion of the CMB blackbody spectrum, may be absorbed and re-emitted, thereby exciting and de-exciting spin-flip transitions. When radiative interactions with the radio background dominate, a thermal equilibrium is established between the spin temperature and the temperature of the radio background T_γ. In this situation, the spin temperature is said to be strongly coupled with the radio background temperature, meaning $T_S \to T_\gamma$.

Secondly, when the gas density is high collisions between two hydrogen atoms, a hydrogen atom and an electron, or even a hydrogen atom and a proton become common. The kinetic energy transfer during these collisions may induce a spin-flip transition in the involved hydrogen atoms. In high density regimes where collisions are the dominant interaction, the spin temperature is pulled towards an equilibrium with the gas kinetic temperature T_K. The spin temperature becomes strongly coupled with the kinetic temperature of the gas and $T_S \to T_K$ (Pritchard & Loeb, 2012).

Finally, external Lyα radiation also influences the spin temperature via the Wouthuysen-Field effect (Wouthuysen, 1952; Field, 1958). The Wouthuysen-Field effect describes the process through which a Lyα photon is absorbed by a neutral hydrogen atom in one hyperfine state and then re-emitted with the atom settling to the other hyperfine state. The net effect is that the hydrogen atom undergoes a spin-flip transition and this mechanism brings the spin temperature to an equilibrium with the color temperature T_α. Moreover, the color temperature is closely coupled to the gas kinetic temperature due to Lyα scattering, which means that $T_S \to T_\alpha \approx T_K$.

Having established the mechanisms that impact the spin temperature, we can now proceed to outline the evolution of the 21-cm signal throughout the early universe. Due to quantum inhomogeneities that arose during inflation, the neutral hydrogen gas in the early universe was non-uniformly distributed throughout space. Therefore, the observed brightness temperature of the 21-cm signal fluctuates as we go from overdense to underdense regions. A simulation showing spatial fluctuations in the 21-cm signal is displayed in the top panel of Figure 1.1. Concurrently,

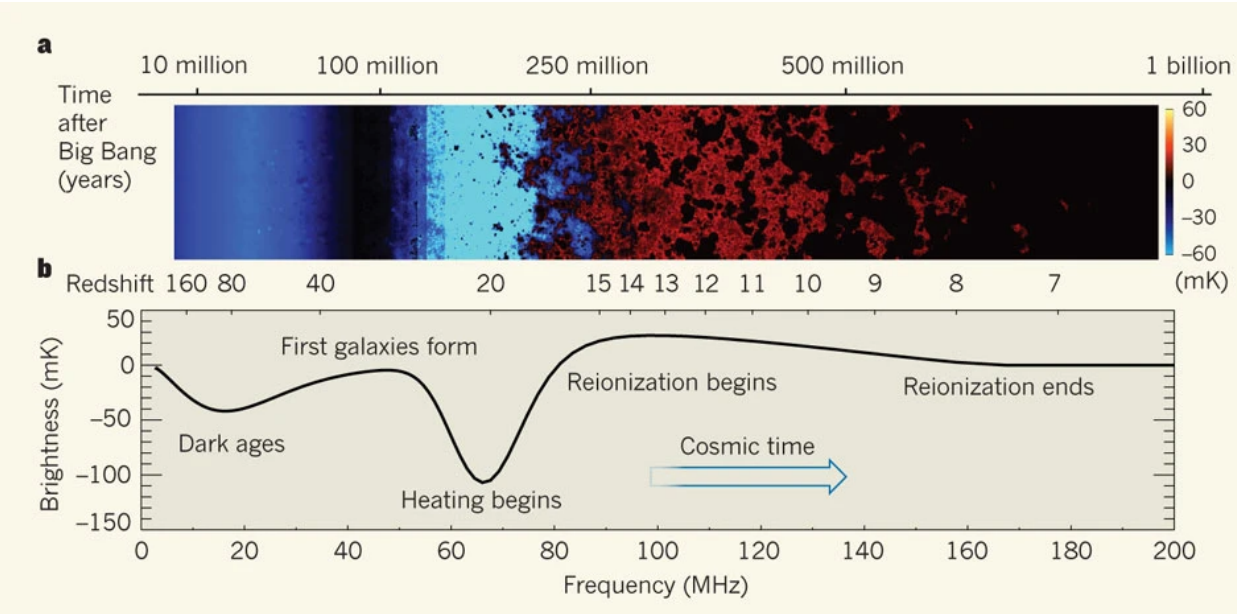

Figure 1.1: (a) Simulation result showing the time evolution of spatial fluctuations in the 21-cm brightness temperature from the cosmic dark ages to the end of the epoch of reionization. **(b)** Illustration of the expected sky-averaged 21-cm signal over the same time period (Pritchard & Loeb, 2010).

the bottom panel of Figure 1.1 illustrates the expected form of the global 21-cm signal, which is obtained by averaging over the spatial fluctuations.

As seen in the Figure 1.1, at first, there was no global signal ($\delta T_b = 0$) because the temperature of the CMB and the kinetic temperature of the neutral hydrogen gas had remained radiatively coupled after recombination and decoupling, while the high density environment caused the spin temperature to be collisionally coupled to the kinetic gas temperature. Thus, $T_{\rm CMB} = T_K = T_S$ and no 21-cm signal could be observed. However, as the universe expanded, the CMB cooled as $T_{\rm CMB} \propto 1+z$ while the gas cooled adiabatically as $T_K \propto (1+z)^2$. Around $z \sim 200$, the gas thermally decoupled from the background radiation, and so the gas kinetic temperature fell below the CMB temperature. Since the spin temperature was still collisionally coupled to the gas, we have $T_S < T_{\rm CMB}$, meaning that the 21-cm signal became observable in absorption. Eventually, the continual expansion of space caused the gas density to dilute to the point that collisional coupling was no longer effective compared to radiative coupling. As such, the spin temperature became coupled with the background radiation such that $T_S = T_{\rm CMB}$ and the 21-cm signal disappeared.

This sequence of events occurred during the cosmic dark ages and produced the first absorption trough in the global 21-cm signal which can be seen for $z \gtrsim 40$ in Figure 1.1.

The next disruption of the global 21-cm signal was caused by the birth of the first stars. Following cosmic dawn, stars began to emit Lyα and X-ray photons, which again resulted in the spin temperature coupling to the kinetic temperature of the gas. This time the coupling mechanism was due to Lyα interactions and the Wouthuysen-Field effect. Once more, $T_S < T_{\rm CMB}$ and the 21-cm signal appeared as a new absorption trough. Meanwhile, stellar radiation began to heat the gas. At some point, the effect of Lyα coupling saturated and the spin temperature began to rise as it was coupled to the warming gas. It may have risen beyond the temperature of the radio background such that $T_S > T_{\rm CMB}$, leading the 21-cm signal to be observed in emission. During the epoch of reionization, X-ray sources ultimately reionized the hydrogen gas which significantly diminished the cosmological 21-cm signal (Pritchard & Loeb, 2012). The absorption trough for cosmic dawn is shown between $30 \gtrsim z \gtrsim 15$ in Figure 1.1 while the potential emission feature and gradual decay of the global signal can be seen at $15 \gtrsim z \gtrsim 6$.

1.2.3 Spatial fluctuations

In reality, for a given redshift z, the brightness temperature of the 21-cm signal fluctuates in pockets around overdense and underdense regions of the early universe. The sky-averaged global signal does not convey information about the interesting physics of these spatial fluctuations. Instead, one can study these fluctuations using tomography whereby hydrogen in the early universe is viewed in three dimensions: two spatial dimensions and one dimension in frequency/redshift. Two-dimensional maps of the 21-cm signal, like Figure 1.2a, at many redshifts would reveal the evolution of fluctuations in the 21-cm signal.

Modelling 21-cm fluctuations is simplest during the cosmic dark ages. Throughout this period, fluctuations in the 21-cm signal are sourced by inflationary inhomogeneities where there are local variations in the density of hydrogen. Dark ages 21-cm fluctuations are therefore able to directly probe cosmological properties and contain an unprecedented amount of cosmological information (Loeb & Zaldarriaga, 2004).

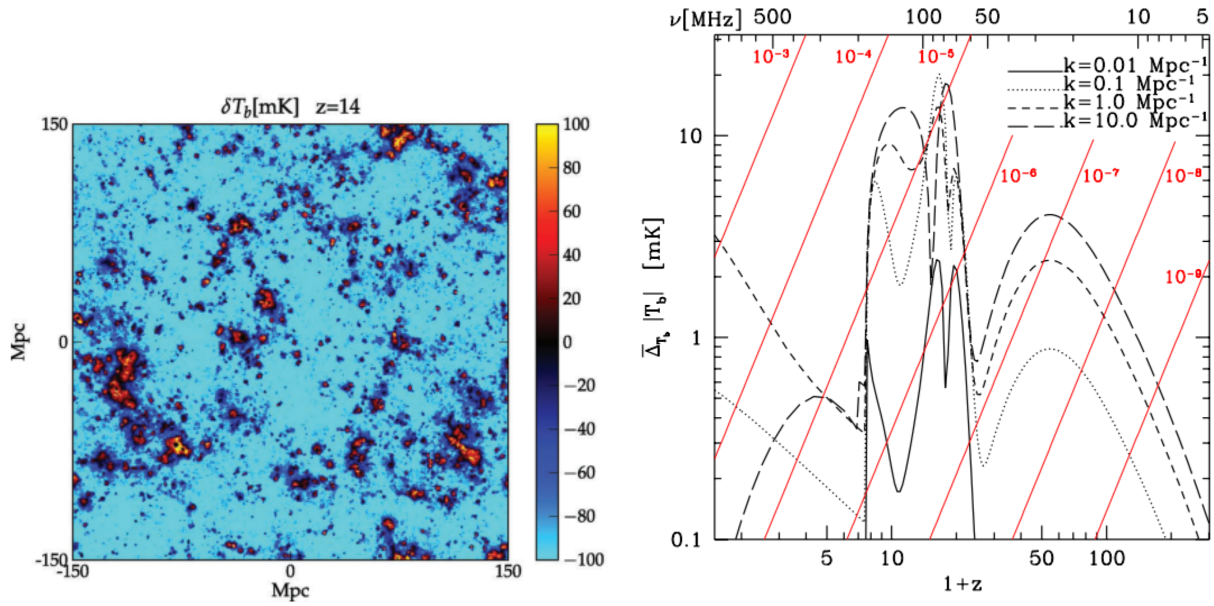

(a) (b)

Figure 1.2: **(a)** Spatial fluctuations in a simulated 21-cm brightness temperature map at redshift $z = 14$ (Santos et al., 2010). **(b)** Model of the 21-cm power spectrum's evolution as a function of redshift $1+z$ for some constant values of k. The red diagonal lines indicate the magnitude of foreground removal required to detect the 21-cm signal (Pritchard & Loeb, 2008).

From cosmic dawn and beyond, the 21-cm signal is complicated by local variations in ionization, Lyα coupling, and gas temperature around astrophysical structures. Localized fluctuations in the above cause subsequent spatial fluctuations in the 21-cm brightness temperature. Also, the peculiar velocity of a neutral hydrogen cloud can anisotropically distort the frequency–redshift conversion in Equation 1.2 as the bulk motion of the cloud along the line of sight leads to additional redshifts or blueshifts, depending on the flow direction (Pritchard & Loeb, 2012).

Spatial fluctuations in the 21-cm signal are often discussed in Fourier space where k is the comoving wavenumber that is large for small-scale fluctuations in space and small for large-scale fluctuations. The power spectrum P_{T_b} is defined by

$$\left\langle \delta_{T_b}(\mathbf{k})\delta^*_{T_b}(\mathbf{k}')\right\rangle = (2\pi)^3\delta_D(\mathbf{k}-\mathbf{k}')P_{T_b}(k), \tag{1.10}$$

where $\delta_{T_b}(\mathbf{k})$ is the Fourier transform of the 21-cm signal fluctuations, and δ_D is the Dirac delta function (Cohen et al., 2018). It is an important tool for studying the statistics of the fluctuations and an example model of the 21-cm power spectrum as a function of redshift is shown in Figure 1.2b. A peak at $z \approx 50$ is visible for all k modes as the power spectrum mimics the dark ages absorption trough of the global signal modulated by the growing scale of the density fluctuations. At later times, the power spectrum has many peaks owing to the complicated astrophysics at play until the end of reionization when the 21-cm signal disappears. (Pritchard & Loeb, 2012).

1.3 Observing the redshifted 21-cm line at low frequencies

1.3.1 Frequencies of interest

The observational frequencies required to access a particular window of the 21-cm signal can be calculated using Equation 1.2 along with the estimated redshift range of the relevant epoch. The dark ages, which occurred between $1100 \gtrsim z \gtrsim 30$, correspond to frequencies from about 1.3 to 50 MHz. Cosmic dawn is thought to have lasted from $z \sim 30$ to ~ 15 and corresponds to relatively higher frequencies between approximately 50 and 90 MHz. Finally, the 21-cm signal from the epoch of reionization could be observable up to $z \sim 6$, or approximately 200 MHz. Since the signal covers such a wide range of frequencies, instruments in 21-cm cosmology experiments are designed to be suitably broadband.

1.3.2 Observational challenges

The low frequencies involved in 21-cm cosmology experiments are challenging to observe for a number of reasons including strong Galactic foregrounds, ionospheric interference, and radio-frequency interference from human activity.

Galactic foregrounds: Strong radio emission from Galactic and extragalactic sources obfuscate the cosmological 21-cm signal. These foregrounds are mainly Galactic synchrotron emission and Galactic free-free emission, and the spectrum follows a power law with a spectral index of ~ 2.8 (Platania et al., 1998). The Galactic foregrounds are many orders of magnitude brighter than the 21-cm signal and get even brighter for decreasing frequencies. This means that foreground radiation is particularly strong at the observable frequencies for the cosmic dark ages. Additionally, although the spectral index and spatial distribution of the foregrounds are consistent for most frequencies of interest, the spectrum turns over below $\sim 3\,\mathrm{MHz}$ and the morphology of the foregrounds changes drastically due to free-free absorption in the Galactic plane (Cong et al., 2021). In all cases, these foregrounds are unavoidable and must be accurately removed from the data in order to assess the cosmological information contained inside measurements of the redshifted 21-cm line (Huang et al., 2018; Liu & Shaw, 2020).

Ionospheric interference: Free electrons in Earth's ionospheric layer also interfere with 21-cm observations of the early universe as they scatter incoming radiation at radio frequencies. Lower frequencies experience a higher and more turbulent degree of scattering, which increasingly distorts the measured signal, until the ionosphere becomes completely opaque below the plasma cutoff frequency. The ionosphere is primarily ionized by UV radiation from the Sun, and fluctuations in solar radiation cause the cutoff frequency to vary in both time and location. A typical value for the plasma cutoff frequency is $\sim 30\,\mathrm{MHz}$, but it is reduced at times when solar radiation is weak, like at solar minima and polar night. Therefore, the best viewing conditions for ground-based observations of the radio sky are during a solar minimum as well as during winter at polar latitudes.

Radio-frequency interference (RFI): Radio broadcasting stations and other transmitters commonly use frequencies that interfere with the redshifted 21-cm signal. These human-made signals can be many orders of magnitude stronger than even the Galactic foreground and directly obstruct the 21-cm signal at the same frequencies. Frequencies other than the transmission frequency can also be overwhelmed by RFI because of intermodulation, leakage, and overloading. To avoid RFI contamination, a radio-quiet observing site that is extremely remote or well shielded by mountainous terrain should be chosen. But even then, aircraft and meteors can reflect RFI from distant transmitters towards the radio telescope, while telecommunications from satellites are an unavoidable RFI source to any ground-based observations regardless of location. Alternatively, an experiment located on the far side of the Moon, either on the lunar surface as proposed for the FARSIDE mission (Burns, 2021) or in lunar orbit like the Netherlands China Low Frequency Explorer (NCLE; Bentum et al., 2020), would be exceptionally well shielded from terrestrial RFI while simultaneously avoiding ionospheric contamination (Jester & Falcke, 2009). Still, RFI can be self-generated by the instrument's own electronics if they are not properly shielded. Any RFI that appears in the measurements must be flagged and removed during data analysis (Liu & Shaw, 2020). With that being said, some types of RFI can be beneficial. For example, the ORBCOMM satellite constellation at 137 MHz can be used to calibrate the beam pattern of an antenna (Neben et al., 2015; Line et al., 2018).

1.4 Overview of 21-cm cosmology experiments

Different types of experiments can measure different aspects of the 21-cm signal. For example, the global signal can be measured by a single antenna that observes the brightness temperature of the full sky. On the other hand, large interferometric radio arrays consisting of many antennas will be necessary to spatially resolve 21-cm fluctuations.

1.4.1 Global signal experiments

The Experiment to Detect the Global EoR Signature (EDGES) is a global 21-cm experiment located at the radio-quiet Murchison Radio-astronomy Observatory in Australia. The EDGES experiment uses a blade dipole antenna design that operates in two frequency bands: 50–100 MHz and 90–100 MHz. In 2018, EDGES became the first and only experiment thus far to report the potential detection of the global 21-cm signal. It found an absorption feature centred at 78 MHz with a width of 19 MHz and an amplitude of 0.5 K (Bowman et al., 2018). Strikingly, the measured absorption trough's amplitude is more than two times larger than anticipated by even the most extreme models. The discrepancy suggests that either the intergalactic gas was much colder than previously thought, or that the brightness temperature of the radio background was higher than models predicted. It is currently unclear how this situation might arise, but some theories invoking exotic physics have been proposed. One such idea states that interactions between baryons and dark matter could have caused the gas temperature to be cooler than originally expected (Barkana, 2018). Another analysis of current radio sky maps shows support for a background radiation field in addition to the CMB (Dowell & Taylor, 2018). At this time, independent confirmation of the EDGES absorption feature is critical to our understanding of the universe. As such, several global 21-cm experiments are attempting to confirm the validity of the EDGES detection, each using a different of instrumental design as a way to prevent the reproduction of systematic errors. The list of ongoing global 21-cm experiments includes SARAS (Singh et al., 2018; Nambissan T. et al., 2021), PRIZM (Philip et al., 2019), MIST (Hendricksen, 2021), LEDA (Price et al., 2018), CTP (Nhan et al., 2018), REACH (de Lera Acedo, 2019), High-Z (Peterson, 2021), and the LWA-SV (Dilullo et al., 2020).

1.4.2 Low-frequency experiments

Due to increased ionospheric interference, low frequencies $\lesssim 30\,\mathrm{MHz}$ are the most difficult for observing the radio sky. For that reason, there is a severe lack of observational data available below 30 MHz. To date, only a small number of ground-based low-frequency experiments with poor resolution were performed in Australia and Canada during the 1960s and 1970s (Cane & Whitham, 1977; Ellis & Hamilton, 1966; Mathewson et al., 1965; Caswell, 1976; Roger et al., 1999). Most notably, at the very lowest frequencies, Reber (1968) mapped the southern sky with a resolution of 7° at 2.1 MHz, as shown in Figure 1.3, using an array of 192 dipoles arranged in a 1-kilometre-wide circular area, while Ellis & Mendillo (1987) were able to map the 1.6 MHz sky at a resolution of 25° using an array of eight 180 m dipoles and just eleven nights of observing time with sufficiently low levels of ionospheric interference. Meanwhile in space, the Radio Astronomy Explorer-2 satellite studied Galactic emission below $\sim 10\,\mathrm{MHz}$ from lunar orbit with meagre $\sim 30^\circ$ resolution or worse (Novaco & Brown, 1978). On the ground, the current batch of modern low-frequency experiments includes the NenuFAR array in France, which operates between 10–85 MHz with 3° resolution at the low end of its band (Zarka et al., 2015) and the Ukrainian T-shaped Radio telescope, which observes between 8–32 MHz with 0.5° resolution at the centre of its band (Zakharenko et al., 2016). So far, the lowest frequency at which a high-resolution image of Galactic radiation has been made is 36.5 MHz. It was imaged at a resolution of $15'$ by the Owens Valley Long Wavelength Array (Eastwood et al., 2018). A few space missions have also been proposed to realize modern high-resolution full-sky maps at low frequencies, unobstructed by ionospheric interference: Discovering the Sky at the Longest wavelengths plans to launch a constellation of satellites into lunar orbit to observe below 30 MHz (Chen et al., 2019) and the FARSIDE experiment is proposing to install of a radio array on the lunar surface that would operate below 40 MHz (Burns et al., 2019).

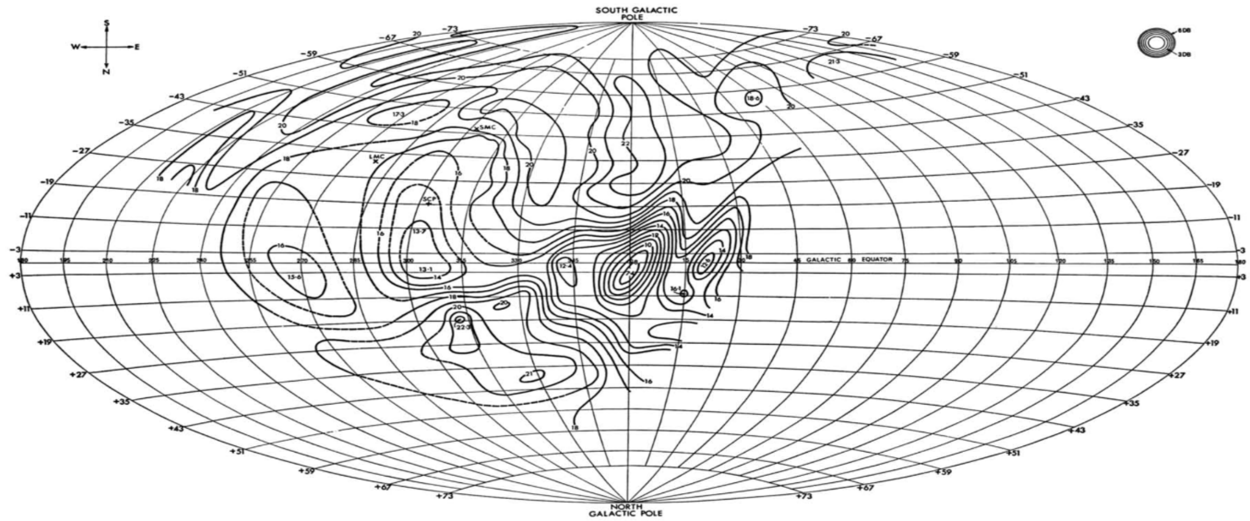

Figure 1.3: The current state-of-the-art map of the low-frequency radio sky. The map gives contours of Galactic radiation at 2.1 MHz and with a resolution of 7.1°. The South Galactic pole is at the top. Figure taken from Reber (1968).

1.5 Thesis outline

The main topic of this thesis will be the ALBATROS experiment, a new radio telescope aiming to map the low-frequency sky and take first steps towards future observations of the dark ages 21-cm signal. In Chapter 2, I will introduce the ALBATROS experiment, including its goals, specifications, and some results up to now. Many recent improvements to the experiment's hardware as well as ongoing development on a low-frequency antenna and pre-amplifier will be discussed here. In Chapter 3, I will present a computational tool that I developed to map the propagation of RFI noise over real terrain and help discover new radio-quiet sites. Then, in Chapter 4, I will discuss preliminary results of the first autonomous two-element array that was installed at a new radio-quiet test site in northern Québec. This site was selected based on the RFI predictions described in the previous chapter. Finally, Chapter 5 will conclude with an outlook on the future of the ALBATROS project.

Chapter 2

ALBATROS low-frequency interferometer

ALBATROS is a new experiment with the ultimate goal of laying the groundwork for future scientific explorations of the cosmic dark ages. It will do so by taking the first high-resolution images of the radio sky below 30 MHz, where there is a true dearth of observational data. Modern high-resolution maps of Galactic foregrounds at low frequencies, like those provided by ALBATROS, will be crucial to the success of the first generation of dark ages cosmology experiments. In fact, foregrounds are brightest in the frequency range corresponding to the dark ages and, compared to other windows of the 21-cm signal, will require particularly careful modelling in order to extract the desired cosmological signal.

ALBATROS will consist of a small number of autonomous antenna stations operating at 1.2–125 MHz that form interferometric arrays installed at several different locations. The autonomous antenna stations will record and store data independently from one another. The data will subsequently be retrieved, physically, from the site and correlated in post-processing. The frequency span of ALBATROS extends to 125 MHz so that aliased ORBCOMM signals are observed in the operational band, thereby allowing for refined synchronization of the collected data from each antenna station during the offline correlation process. As the antenna stations function fully autonomously, they can be separated from one another by large distances. In this way, the resulting array can achieve high resolution imaging on the order of several arcminutes at frequencies below ~ 10 MHz. Baseline distances of ~ 10 km will allow ALBATROS to attain an order of magnitude improvement in resolution compared to previous experiments at $\lesssim 30$ MHz. To further improve observations, the sites of potential ALBATROS arrays are chosen specifically for their favourable ionospheric conditions and exceptional radio-quiet environment.

In this chapter, I will provide an overview of the current state of the ALBATROS experiment, including its installations and components. The ALBATROS instrument was previously described in Chiang et al. (2020). Here, I will introduce various new developments to the experiment's hardware, such as upgraded back-end electronics as well as new power and data storage systems. This chapter will also discuss the development of new antenna and low-noise amplifier designs for improved performance at low frequencies. However, these designs are still evolving and represent an active area of development at the time of writing.

2.1 Installation sites

The sites of ALBATROS arrays are selected based on their local RFI environment and ionospheric conditions. To minimize contamination from human-made RFI, a potential site must be sufficiently distant and isolated that unwanted signals from radio transmitters are insignificant. Also, polar and near-polar sites are preferred for their reduced ionospheric activity, especially during winter. As such, ALBATROS array sites are located near or at high latitudes, in very remote and radio-quiet locations. Another consideration of importance for the installation site of a radio interferometer is its accessibility. In many instances, accessibility and radio-quietness are in conflict with one another as more-readily accessible sites tend to be closer to civilization, and thus sources of RFI.

So far, antennas have been installed at three different sites: Marion Island, the McGill Arctic Research Station (MARS)[1], and Uapishka Station[2]. The first two are located thousands of kilometres from any large population centres and are extraordinarily radio-quiet. An ALBATROS array is planned to be installed at each of these locations. The last site, Uapishka Station, has significantly higher RFI levels than the other locations, but is considerably more accessible and is sufficiently radio-quiet for testing new ALBATROS systems. The location of all three sites is shown in Figure 2.1.

[1]https://www.mcgill.ca/mars/
[2]https://www.stationuapishka.com/

Figure 2.1: Location of sites where ALBATROS antenna stations have been installed. So far, three antennas were installed on Marion Island in 2018, one antenna was installed at MARS in 2019, and three antennas were installed at Uapishka in 2021.

2.1.1 Marion Island

Marion Island is a subantarctic island located in the southern Indian Ocean. It is about 2000 km from the nearest continental landmass and is uninhabited except for a research station operated by the South African National Antarctic Programme. For these reasons, Marion Island is one the most radio-quiet sites in the world (Philip et al., 2019). Ionospheric conditions on Marion Island are also expected to be favourable for low-frequency observing. In Figure 2.2a, predictions from the International Reference Ionosphere model (Bilitza, 2018) suggest a plasma cutoff frequency reaching as low as ~ 1.5 MHz during the solar minimum in 2007. Due to its remoteness, access to Marion Island is limited. An annual ship voyage to relieve the research station is the only available transportation to the island.

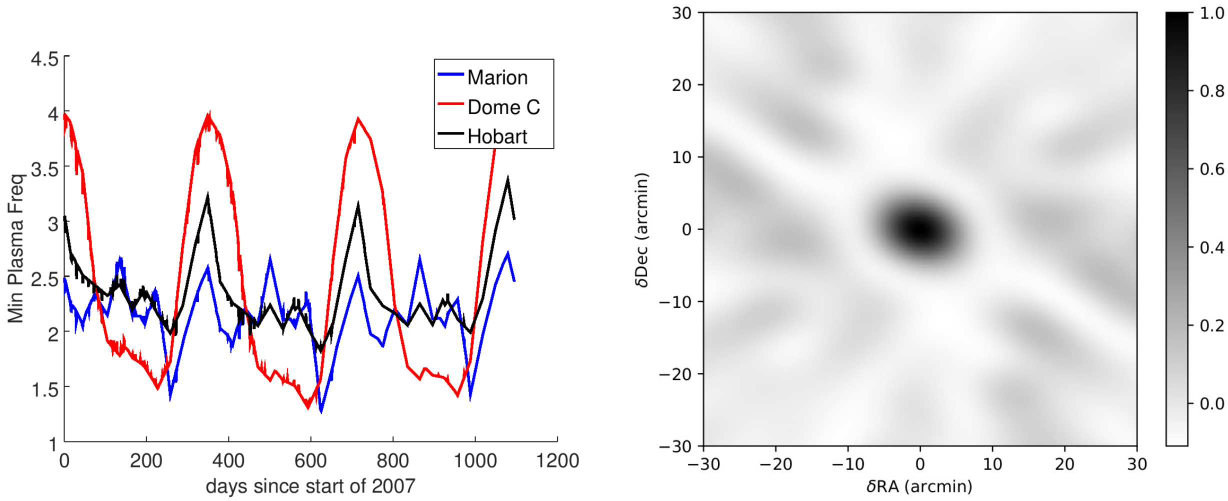

(a) (b)

Figure 2.2: **(a)** Predicted plasma cutoff frequency at Marion Island, Dome C (Antarctica), and Hobart (Tasmania) during solar minimum. Dome C is known to be an excellent radio astronomy site while Hobart is the location from which Reber observed the 2.1 MHz sky. **(b)** Synthesized beam at zenith calculated using an octave of bandwidth centred on 5 MHz and the locations of the ten planned antenna stations on Marion Island. The full width of the beam is calculated to be $\sim 7'$. Both figures taken from Chiang et al. (2020).

The ALBATROS array on Marion Island will observe the southern sky with ten antenna stations situated mostly along the island's perimeter. The proposed arrangement will have a maximum baseline length of about 20 km. In turn, the array at Marion will have a beamwidth of approximately $7'$ at zenith. The synthesized beam shape for this array is displayed in Figure 2.2b. Marion Island is also the site of PRIZM, a 21-cm cosmology experiment that is designed to measure the global signal at cosmic dawn.

2.1.2 McGill Arctic Research Station

MARS is a seasonal research facility located 8 km inland from Expedition Fjord on Axel Heiberg Island in the Canadian High Arctic. The island is also uninhabited most of the year except from April–August when the research station is operational. The nearest populated communities with radio transmitters are hundreds of kilometres away. RFI measurements conducted at MARS in summer 2019 confirm that its environment is exceptionally radio-quiet. In worst-case conditions,

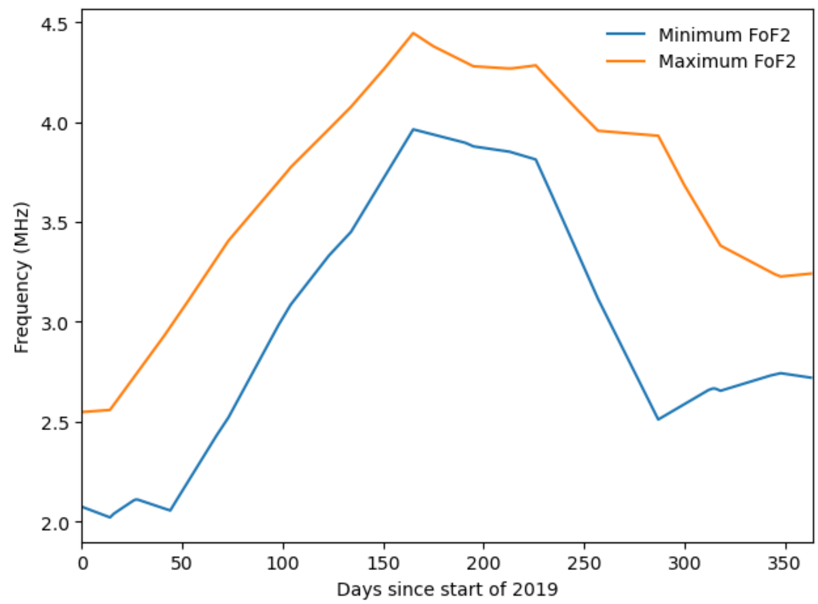

Figure 2.3: Minimum and maximum daily critical frequency for the F2 layer of the ionosphere (FoF2) at MARS during the most recent solar minimum as predicted by the International Reference Ionosphere model. The plasma cutoff frequency is lowered for extended periods of time during the Arctic winter. Figure courtesy of Jon Sievers.

the overall RFI occupancy rate was determined to be 1.8% in the range of 20–125 MHz (Dyson et al., 2021). Ionospheric interference at the MARS site is expected to be very low relative to other radio-quiet sites around the world. MARS is located well within the Arctic circle and experiences 24-hour darkness during the winter. As shown in Figure 2.3, the plasma cutoff frequency at MARS is expected to be diminished during polar night, thereby enabling extended periods of observation on the sky at very low frequencies. Similarly to Marion Island, access to MARS is limited by harsh weather and difficult logistics.

The initial plan for the ALBATROS array at MARS involves the installation of six autonomous antenna stations for observing the northern sky. The proposed antenna installation sites are displayed in Figure 2.4a and the maximum baseline length in the array will be approximately 10 km. As demonstrated in Figure 2.4b, this array configuration will result in a beamwidth of $\sim 12'$ at 5 MHz. The slightly larger beamwidth compared to the proposed array on Marion Island is consistent with the fact that fewer antennas and shorter baselines will be used at MARS.

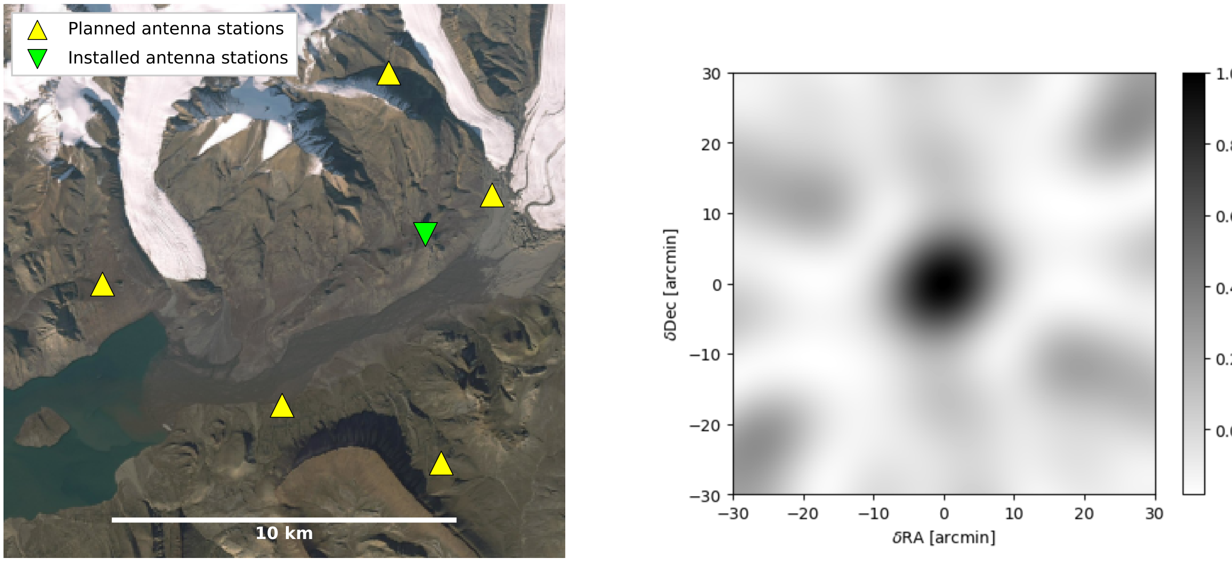

(a) (b)

Figure 2.4: **(a)** Satellite image of Expedition Fjord showing potential sites for antenna stations. The longest baseline between antenna stations is projected to be just over 10 km. One antenna has already been installed at MARS and its location (in green) is near the base camp. **(b)** Synthesized beam at zenith using the six proposed antenna sites at MARS. Using an octave of bandwidth centred on 5 MHz, the full width of the beam is $\sim 12'$.

2.1.3 Uapishka Station

The final site used by ALBATROS is Uapishka Station, a research base on the shore of the Manicouagan reservoir in northern Québec. The closest populated centres are Fermont (170 km northeast), Sept-Îles (190 km southeast), and Baie-Comeau (250 km south). Also, there are a number of hydroelectric power stations in the vicinity: the Manic-5 station is 100 km to the south while the Hart-Jaune station is 40 km to the northeast. Fortunately, the area around Uapishka Station is mountainous which provides additional shielding from RFI sources and, importantly, there are no power lines in the general area. Cursory surveying of the area established that many locations near the station are acceptably radio-quiet for the purpose of testing ALBATROS equipment. The station is accessible year-round by road via Québec's Route 389 and the trip from McGill University in Montréal takes approximately twelve hours by car. Uapishka Station is much more accessible than both Marion Island and MARS, and therefore makes an excellent test site for ALBATROS instrumentation. In 2021, three antennas were installed at a site situated approximately 800 m south of the main base as part of the first deployment to Uapishka. The setup of these antennas will be described in greater detail in Section 4.1.

2.2 Autonomous antenna station

Due to the limited accessibility and harsh climates encountered at Marion Island and MARS, ALBATROS equipment must be designed to operate unattended for extended periods of time while enduring extreme weather conditions. A completed ALBATROS array will consist of several physically robust and autonomously-operating antenna stations. Each antenna station will be comprised of a dual-polarization dipole antenna, active front-end electronics, back-end electronics, a large data storage system, and a power supply system. Each of these subsystems will be described in the following sections. The detailed block diagram of an ALBATROS autonomous antenna station is displayed in Figure 2.5.

2.2.1 Antenna

ALBATROS currently employs a Long Wavelength Array (LWA) dual-polarization dipole antenna. The two dipoles that form the antenna are arranged orthogonally and each has a "tied fork with crosspiece" design that is low cost and physically robust. This antenna was developed for use in the Long Wavelength Array (Hicks et al., 2012). It is well characterized, readily available off-the-self, and easy to install.

The intended operation range of the LWA antenna is between 20–80 MHz. At low frequencies, measurements using the LWA antenna are hindered by a significant drop-off in the antenna's response. Figure 2.6 shows an example of the measured autospectrum recorded with an LWA antenna dropping by an order of magnitude between $\sim$ 15–30 MHz. Therefore, I performed many simulations of the LWA antenna as a way of better understanding the antenna's electrical behaviour below 30 MHz, where ALBATROS efforts are focused.

To start with, the antenna is electrically small at low frequencies and its beam pattern is thus omnidirectional and largely achromatic. The LWA antenna has low gain as illustrated in Figure 2.7, where the peak zenith-directed gain is 3.8 dB at 56 MHz. Between 1.2–30 MHz, the gain drops by 38 dB. In comparison, the drop in realized gain, which additionally accounts for impedance

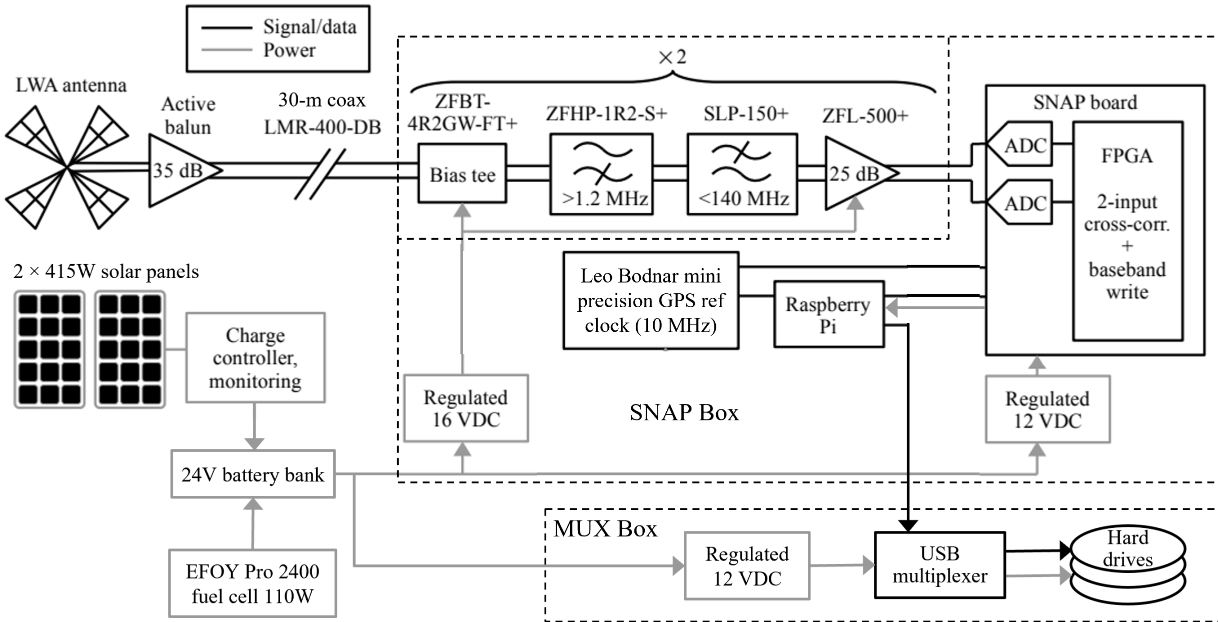

Figure 2.5: Block diagram of an ALBATROS autonomous antenna station. Signals are received by a dual-polarization LWA antenna and amplified by an active front-end balun. The signals from each polarization are sent over coaxial cables to a Faraday cage (dashed box) containing the back-end electronics. Here, the signals go through a chain of RF filters and amplifiers before being digitized by a SNAP board. An on-board FPGA also computes correlations between the two polarizations. The SNAP is controlled by a Raspberry Pi, which also stores the correlated data products. A second Faraday cage houses a set of hard drives and a USB multiplexer, which ensures that baseband data is saved to a drive with free space. Power is supplied by a hybrid methanol-solar system.

mismatch losses between the antenna and its load, is much greater than the drop in gain alone. The realized gain peaks at 1.4 dB at 37 MHz, and by 1.2 MHz it has dropped by nearly 77 dB. The sharp drop-off in the simulated realized gain coincides with the drop-off in the measured response, suggesting that impedance mismatch losses severely affect the performance of the LWA antenna at low frequencies. As a result, work is currently underway to design a new antenna that is optimized for frequencies below 30 MHz. Some of this work will be described in Section 2.4.

Using simulations, I also investigated the effect of a ground screen on the low-frequency behaviour of the LWA antenna. Ground screens are often beneficial because they reduce the variable coupling between the antenna and the soil it sits on. However, measurments of similar antennas demonstrate that this effect is lessened at lower frequencies (Paravastu et al., 2007). I therefore

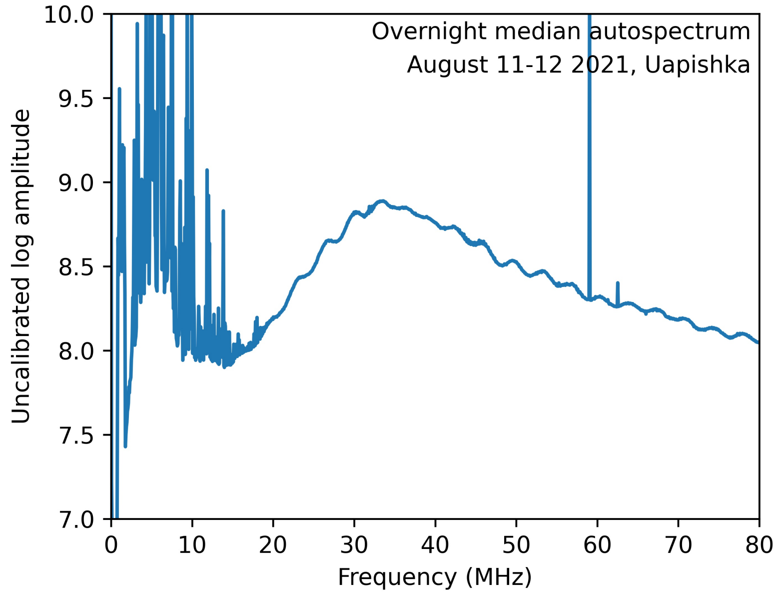

Figure 2.6: Median uncalibrated autospectrum measured overnight with one polarization of an LWA antenna. The response of the LWA antenna drops off noticeably below $\sim 30\,\mathrm{MHz}$. The cruft below $\sim 15\,\mathrm{MHz}$ is mostly shortwave radio below the plasma cutoff frequency. The regular ripples seen clearly in the measured autospectrum above $20\,\mathrm{MHz}$ are caused by reflections in the 30-m coaxial cable between the antenna and the back-end enclosure.

simulated the LWA antenna above a variety of ground screens, including a mesh ground screen that is used at the Long Wavelength Array, radial grounding wires that were temporarily installed with an LWA antenna at MARS, and without a ground screen at all. The zenith-directed realized gain for all these situations is shown in Figure 2.8. The simulations suggest that the realized gain of the LWA antenna below $20\,\mathrm{MHz}$ is slightly higher when used without a ground screen, especially when compared to the mesh ground screen. These simulations only sample a small population of potential ground screens so they are not fully conclusive. Future simulations that vary the ground type as well as the ground screens' dimensions will help identify the optimal ground screen setup for low-frequency measurements. Nonetheless, in my simulations, the impact of the ground screen on the antenna's low-frequency response is negligible, or even slightly adverse. Therefore, the decision was taken to not put down ground screens with the LWA antennas installed at Uapishka Station.

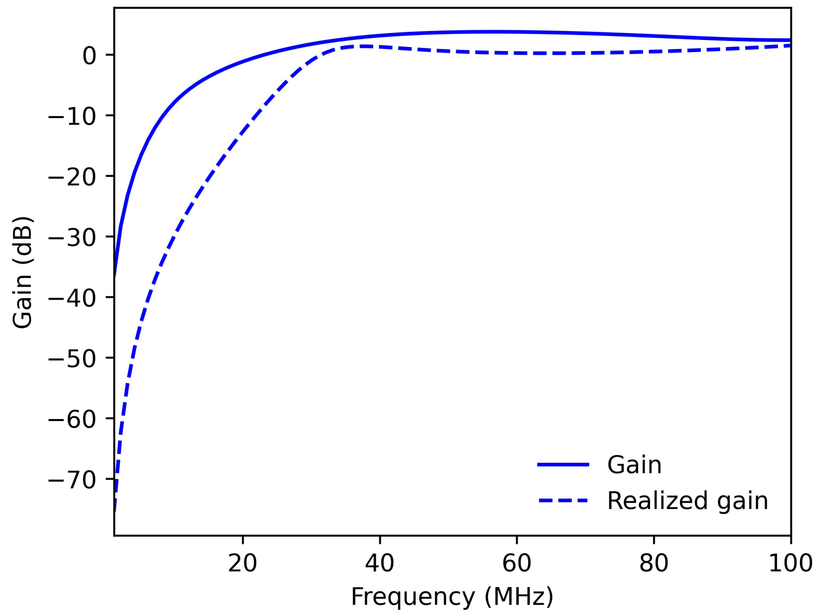

Figure 2.7: Simulated gain and realized gain of the LWA antenna at zenith. The difference between the antenna gain and realized gain comes from the large impedance mismatch at low frequencies. The simulation was done using FEKO, where the LWA antenna was modelled without a ground screen and above average soil with relative permeability of 13 and conductivity of 0.005 S/m. The input impedance of the front-end was set to 100 Ω.

2.2.2 Front-end electronics

In combination with each LWA antenna, ALBATROS uses a LWA active-balun front-end electronics (FEE) revision 1.8 unit. The LWA FEE for dual polarizations is made up of two identical printed circuit boards, each with a conductive ground plane on their backside. The boards are rotated by 90° and stuck back-to-back such that the ground planes are sandwiched between both boards. Each LWA FEE circuit presents a 100 Ω input impedance to the antenna and amplifies received signals by a total of 35.7 dB. Amplification is split into two stages. In the first stage, a pair of GALI-74+ MMIC amplifiers provide 25.1 dB of gain to the input from each dipole arm at a low noise figure of 2.7 dB. The output of the two first-stage amplifiers is differenced by a 180° hybrid coupler whose single output has a 50 Ω impedance. High frequencies are then rejected by a 150 MHz low-pass filter before reaching the second-stage amplifier, a GALI-6+ MMIC with 12 dB of gain and a noise figure of 4.5 dB. The total measured noise figure for the FEE circuit ranges

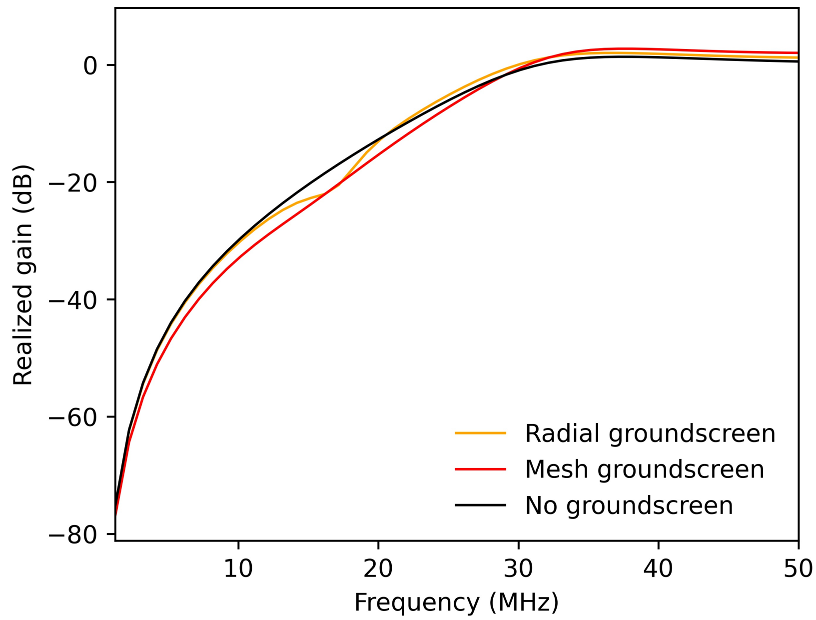

Figure 2.8: Comparison of the realized gain at zenith obtained from FEKO simulations of the LWA antenna modelled with no ground screen, a 10×10 ft mesh wire ground screen with 4×4 in meshing, and a ground screen consisting of eight evenly-spaced radial wires, each 2.9 m in length. Impedance matching is between the antenna source impedance and a 100 Ω front-end.

from 2.74–2.88 dB (Hicks et al., 2012). Each board is powered with 16 V from a bias tee in the back-end electronics enclosure. The combined power consumption for both circuits is about 7 W.

2.2.3 Back-end electronics

A long segment of coaxial cable links the front-end electronics to the back-end electronics, where received radio-frequency (RF) signals are further processed and digitized. All the back-end electronics are placed inside an aluminum enclosure that acts as a Faraday cage to prevent the antenna from picking up self-generated RFI. The enclosure is divided along its midplane by a shelf upon which most of the electronic components are mounted. The topside of the shelf, which is pictured in Figure 2.9a, holds two analog RF signal chains, one for each polarization of the LWA antenna, as well as a Smart Network ADC Processor (SNAP; Hickish et al., 2016), while the underside, which is pictured in Figure 2.9b, carries many control and power modules. I designed and assembled the most recent version of this enclosure, which features a new output terminal for supplying optional

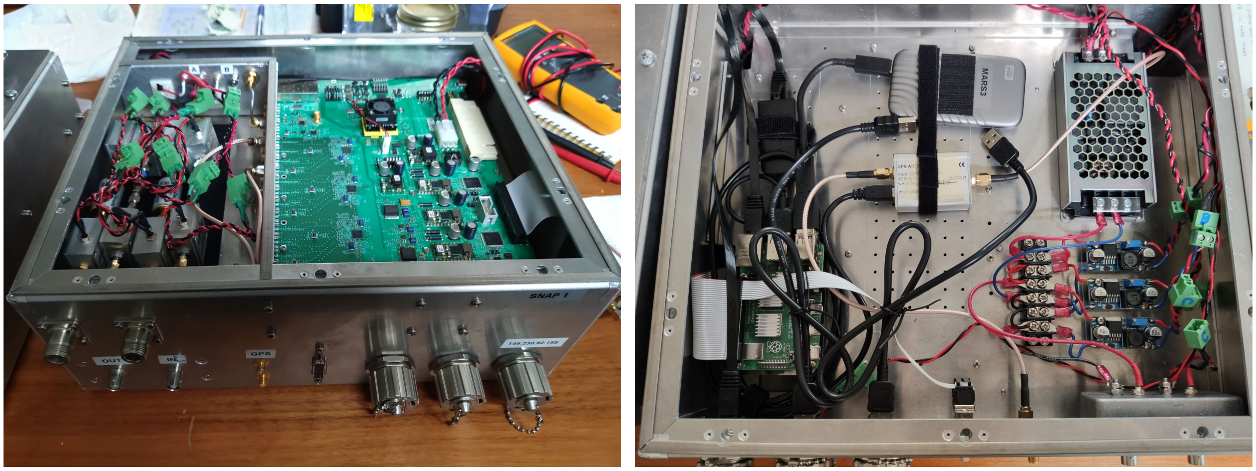

(a) (b)

Figure 2.9: **(a)** Topside and front panel of the Faraday cage that encloses the back-end electronics. Seen here are the RF analog signal chain for each polarization (left) and the SNAP board (right). **(b)** Underside of the back-end electronics enclosure where the Raspberry Pi, Leo Bodnar GPS reference clock, and DC/DC voltage regulators can be seen.

external regulated power, new USB and DB15 ports for communicating with the USB multiplexer described in Section 2.2.4, as well as tweaks to the enclosure's dimensions and organization.

When signals first arrive at the back-end electronics, they are processed by one of the two identical chains of analog RF components. The signal chain consists of a bias tee, a 1.2 MHz high-pass filter, a 140 MHz low-pass filter, and a RF amplifier that provides 25 dB of gain. See Figure 2.5 for the RF components' identification numbers. The RF signal chains are shielded from the rest of the back-end electronics by a partition wall. There is extra space available inside the partitioned area to accommodate the inclusion of additional analog RF components as needed. On the other side of the partition wall, the outputs of the two analog RF processing chains are digitized at 250 Msamp/s by the ADCs on the SNAP board. The signals that are input to the SNAP are channelized into 2048 channels between 0 and 125 MHz, resulting in 61 kHz frequency-wise resolution. The SNAP board also features a FPGA that computes two data products: baseband data for each polarization as well as directly-computed auto- and cross-spectra. Baseband data are sampled at the SNAP board's native sampling rate of 250 Msamp/s for small tunable frequency windows within the range of 0–125 MHz. On the other hand, directly-computed spectra are accumulated over several seconds and encompass the full 0–125 MHz operating range of the SNAP board.

The 140 MHz low-pass filter allows frequencies above the Nyquist frequency to be digitized. Therefore, frequencies between 125–140 MHz will appear aliased in the range of 110–125 MHz. The downlink signal from ORBCOMM satellites, which is regularly broadcast at ~ 137 MHz, is intentionally aliased into the band at ~ 113 MHz for the purpose of precisely synchronizing the timing between autonomous stations.

On the underside of the mounting shelf, there is a Leo Bodnar Mini Precision GPS Reference Clock[3], a Raspberry Pi 4 (RPi) single board computer, a Mean Well DC/DC converter, and three buck converters. The Leo Bodnar reference clock provides a 10 MHz reference signal for ADC synchronization. The RPi is used to control the SNAP board via its GPIO lines. A gigabit ethernet connection is used to transfer baseband data from the SNAP to the RPi at a high data rate. The Mean Well DC/DC converter provides a regulated 12 V source for the SNAP board and a small computer fan that helps circulate air above the power regulators on the SNAP board, while the buck converters provide a regulated 16 V source for the RF amplifiers and bias tees.

2.2.4 Data storage

The ALBATROS autonomous antenna station must be left unattended for long periods of time due to its remoteness. In this time, large amounts of data are collected and must be stored for later retrieval. As previously mentioned, there are two types of data produced by the SNAP board: baseband and directly-computed auto- and cross-spectra. Directly-computed spectra, which are accumulated over several seconds, are gathered at a data rate of $\sim 400\,\mathrm{MB/day}$ (Moso, 2021). The typical length of time that a station would be left unattended is around a year, in which time ~ 150 GB of directly-correlated spectrum data would be collected. This is a relatively small volume of data that can be easily stored on the 256-GB SD card in the RPi. Conversely, baseband data is significantly more voluminous and requires a more intricate data storage solution. The data acquisition software can be configured to record baseband quantized to 1-, 2-, or 4-bits. Higher numbers of bits give higher signal fidelity, but increase the volume of the data. Unlike 1-bit baseband, data quantized at 2- and 4-bits enable the recovery of autospectrum information. However, directly-computed autospectra are saved on a timescale of several seconds and may be used in combination with 1-bit baseband. In benchmark testing, 1-bit baseband data tuned over a bandwidth

[3] http://www.leobodnar.com/shop/index.php?main_page=product_info&products_id=301

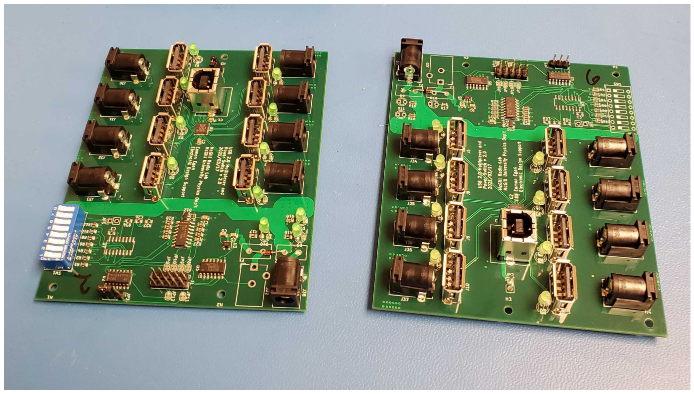

Figure 2.10: Two assembled MUX boards. Each MUX board has enough USB and 12 V power jacks for eight hard drive connections.

of 10 MHz was recorded at a rate of $\sim 0.4\,\mathrm{TB/day}$, or $\sim 150\,\mathrm{TB/year}$. Therefore, a bank of hard drives is connected to the RPi via a USB multiplexer (MUX). The USB multiplexer printed-circuit board, which is pictured in Figure 2.10, was designed by Eamon Egan and allows the RPi to power and enable each connected hard drive individually. In this way, the RPi can shut down a hard drive once it is filled and power on the next one. Only one hard drive needs to be powered at any given time, which reduces the overall power consumption of the autonomous station.

In the field, the MUX boards and hard drive bank are mounted inside another Faraday cage for RF shielding. The enclosure pictured in Figure 2.11 is the first MUX enclosure ever built, which I both designed and assembled. It contains two MUX boards with a total of sixteen 8-TB hard drives, providing a capacity of 128 TB. However, several 12-TB hard drives were recently obtained to further increase the total capacity of the hard drive bank. A full bank of sixteen 12-TB hard drives would provide nearly 200 TB of data storage capacity for each autonomous antenna station. Such a large hard drive bank solves the baseband data storage problem while the MUX ensures that the power draw of the hard drive bank is minimized. Moreover, as larger capacity hard drives become more readily available, the total capacity of the MUX enclosure can easily be scaled up, allowing for baseband data to be recorded over larger bandwidths or at higher bit depths.

2.2.5 Power

At MARS, the best observing period is expected to be during the winter, when the plasma cutoff frequency is reduced and local RFI from human activity is lowest as the research station closes

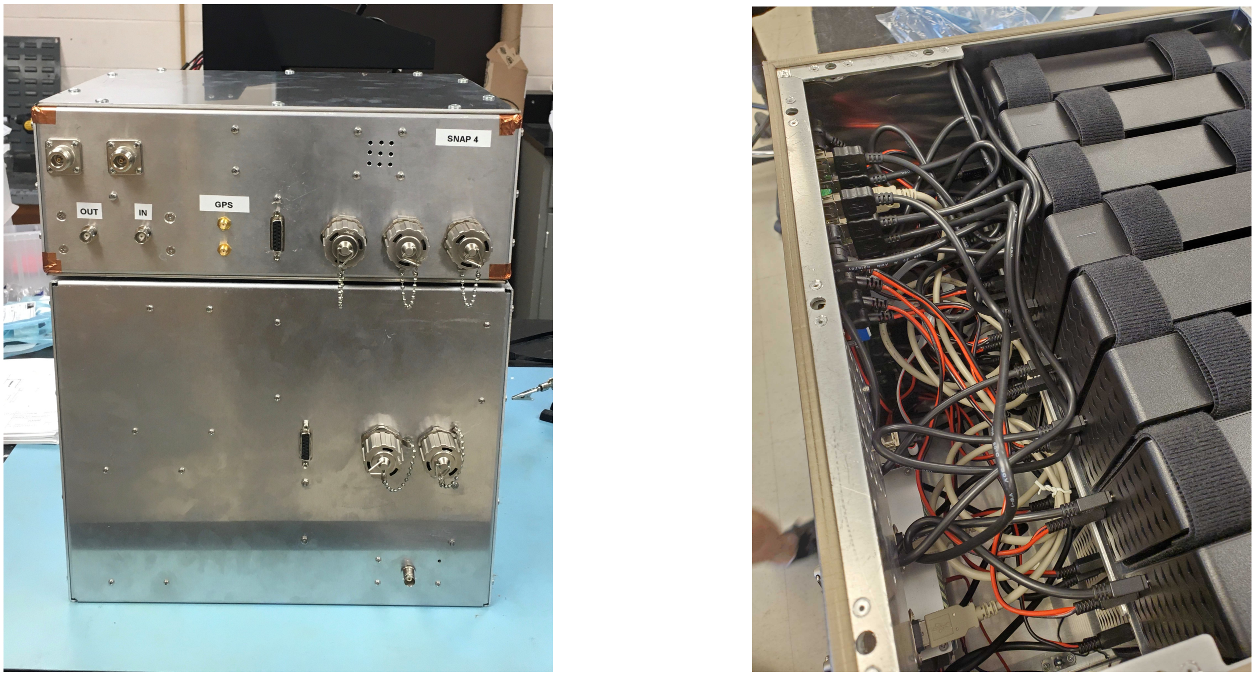

(a) (b)

Figure 2.11: **(a)** Front view of the SNAP enclosure stacked on top of the MUX enclosure. The MUX enclosure has two covered USB input ports and a filtered DB15 input port that allow the RPi in the SNAP enclosure to control the state of the MUX boards and transfer data to the hard drives. An external power input terminal is located near the bottom of the MUX enclosure's front panel for supplying the hard drives with the required DC voltage. **(b)** View inside the assembled MUX enclosure with the top panel removed. A total of sixteen 8-TB hard drives are strapped to both the top and bottom of a central shelf with velcro. Two MUX boards, one for each set of eight hard drives, are mounted to the backside of the front panel. Each MUX board, and in turn each hard drive, is supplied 12 V by a Mean Well DC/DC converter that is also mounted to the backside of the front panel.

until the summer. Solar panels, which are used to power ALBATROS hardware at Marion Island is not feasible at MARS due to polar night. As such, a new power system is required for autonomous antenna station installations in the Arctic. It is difficult to autonomously operate a generator in cold climates, while small wind turbines are ill-suited due to the low wind speeds at MARS. The proposed solution is a hybrid solar-methanol power system that has been specifically designed by SFC Energy, a company specializing in smart fuel cell systems, for extreme climates like the

Arctic. The system uses a EFOY Pro 2400 methanol fuel cell[4], two solar panels, and a 24-V battery bank. During the summer, when the Sun is continually above the horizon, the solar panels provide up to 415 W each, while the methanol fuel cell takes over the power generation duties during the winter and supplies up to 110 W. To compare, I measured the power consumption of the full autonomous antenna station to be ~ 45 W. The EFOY system is fully automatic and is packaged with intelligent control software that keeps the fuel cell in standby mode until the battery actually needs to be charged. To reliably supply an autonomous station for one year, the fuel cell is requires four 60 L methanol cartridges. Due to the very low freezing point of methanol, the cartridges can be exposed to the elements, but the fuel cell and batteries, which are pictured in Figure 2.12a, are kept inside a large thermally-controlled case for environmental protection. The case also has extra room for research equipment, so the dimensions of the back-end electronics and MUX enclosures were specially chosen to fit inside this sheltered space. The command hub of the autonomous station is shown in Figure 2.12b and includes all the data readout and power subsystems.

2.3 Pathfinder experiments

In the past, two proof-of-concept pathfinder experiments were conducted on Marion Island. The first, in 2018, was a two-element array using direct correlation on the SNAP board to determine the feasibility of imaging the low-frequency radio sky from the island. Indeed, the cross-spectrum between two co-aligned polarizations shown in Figure 2.13 demonstrates that fringes due to Galactic emission are seen clearly down to $\lesssim 10$ MHz. This initial ALBATROS pathfinder did not yet feature any autonomous operation capabilities.

The second pathfinder experiment was conducted the next year. Its goal was to establish the technology required for autonomous observations of the low-frequency sky. The first autonomous antenna station prototype was therefore deployed in 2019 and it was powered by an array of nine 110-W solar panels. A similar setup at MARS successfully showcased how baseband data from the dual polarizations of an LWA antenna can be correlated in post-processing to produce auto- and cross- spectra that agree with the directly-computed spectra from the SNAP board. The next step is to correlate baseband data from many autonomous antenna stations, where the relative timing

[4] https://www.efoy-pro.com/en/efoy/efoy-pro-800-2400/

(a) (b)

Figure 2.12: **(a)** EFOY 2400 Pro methanol fuel cell (in light grey) and two series-connected 12-V batteries (in blue) seen inside the thermally-controlled case. **(b)** ALBATROS autonomous antenna station command hub deployed at Uapishka. Seen here are the backsides of two vertically-oriented solar panels, the temperature-controlled case (in dark grey), and four methanol cartridges (below the case). The methanol fuel cell, batteries, back-end electronics, and MUX enclosure are all located inside the case. A custom-built steel structure holds up the case and the solar panels.

between the data acquisition of each station becomes important. Recently, offline correlation of baseband data from two autonomous antenna stations was accomplished for the first time. Preliminary results from this test, which was performed at Uapishka, will be discussed in Chapter 4.

2.4 Low-frequency antenna and FEE development

As noted in Section 2.2.1, the LWA antenna is ill-matched to the low-frequency aspirations of ALBATROS. Despite very bright Galactic emission at low frequencies, the large impedance mismatch between the LWA antenna and its FEE causes a steep drop-off in the measured Galactic signal at frequencies $\lesssim 30\,\text{MHz}$. To address this problem, a new antenna and FEE are now being

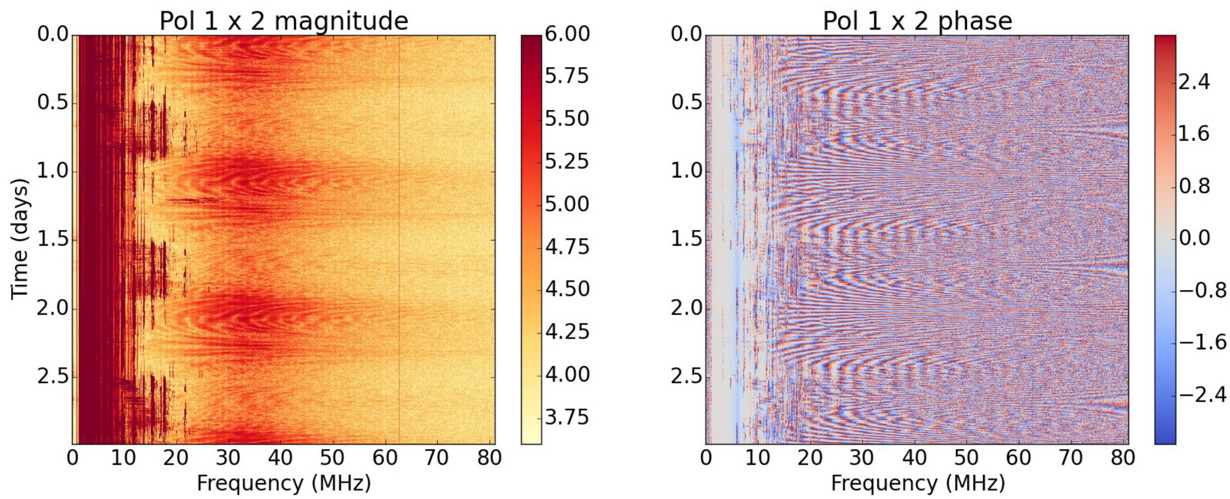

Figure 2.13: Magnitude and phase of the directly-computed cross-spectrum between a pair of co-aligned polarizations in the two-element ALBATROS pathfinder deployed at Marion Island in 2018. The spectra were recorded over three consecutive days and the periodic rise and fall of the Galaxy in that time span is visible in both plots. The magnitude is uncalibrated and logarithmic, while the phase is in radians. Figure taken from Chiang et al. (2020).

developed with the key design criteria being optimized performance in the target frequency range of 1–30 MHz.

Due to the large wavelengths (10–300 m) associated with this frequency range, the new antenna design is forcibly limited to be electrically small. Large resonant or aperture antennas would simply be too costly and difficult to install in the highly remote sites used by ALBATROS. The impedance of an electrically small antenna behaves much like a capacitor, increasing as ν^{-1} for decreasing frequencies. The antenna impedance rises to high values at the lowest frequencies of interest, so the electrically small antenna should be paired with a high input impedance FEE as a way of generally reducing impedance mismatch losses across the band. This sort of design is naturally inefficient but given suitable choices of input impedance and low-noise amplifiers, the bright Galactic signal should still be observable at low frequencies.

Figure 2.14 depicts the electrically small, dual-polarization, inverted vee dipole prototype antenna design that is currently in development. Four wires, two for each polarization, extend downwards from a 10-ft tall vertical mast at an angle of 45° until they reach the half-height of the antenna, at which point guy-ropes pegged into the ground are used to hold the wires in position

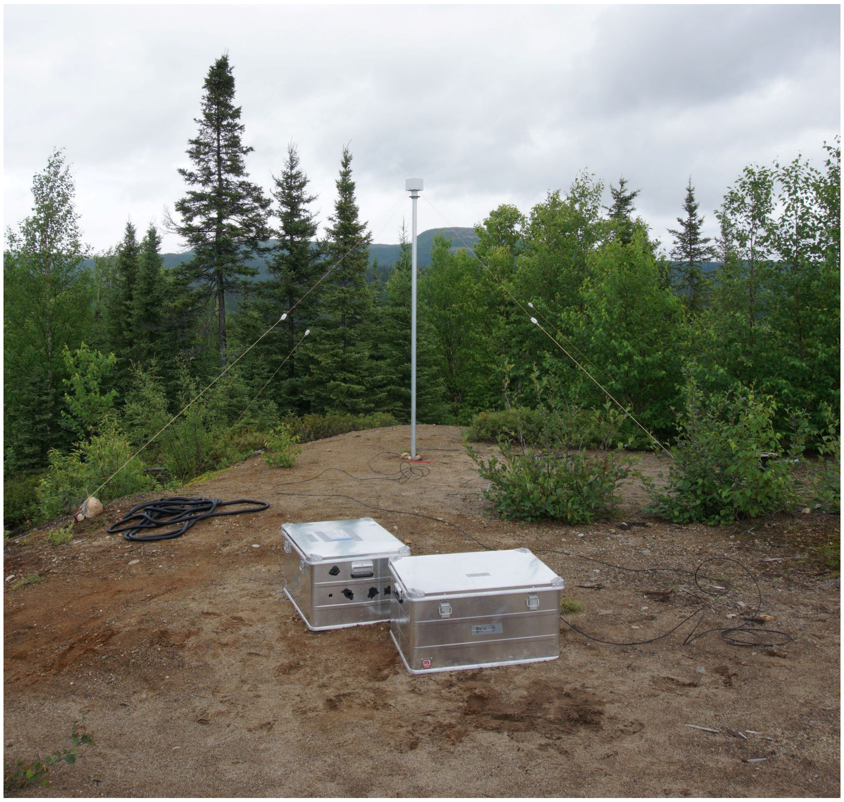

Figure 2.14: Photo of the inverted vee, dual-polarization antenna prototype deployed near Uapishka Station. The FEE is located at the top of the 10-ft vertical mast inside a plastic container for environmental protection. Each dipole arm extends down from the FEE at a 45° angle while tent pegs and guy-ropes hold the structure in place. A 12-V battery and the back-end electronics are sheltered inside the two metal boxes seen in the foreground.

and stabilize the antenna. Each dipole arm is connected to the high impedance FEE board that is affixed to the top of the vertical mast. Compared to the LWA antenna, the new prototype is scaled up in size by a factor of ~ 2, reaching a maximum height of just over 3 m. The advantage of this change is two-fold: (1) the antenna's effective length is increased at low frequencies, allowing better reception of Galactic signal below 30 MHz, and (2) the peak in the antenna's response due to constructive interference between the Galactic signal and its reflection off the ground is pushed to lower frequency by the raised height of the antenna. Optionally, the vertical mast can be constructed out of conductive material which allows for a third polarization measurement from the same antenna.

2.4.1 Simulations of the inverted vee dipole

Using FEKO, I created an antenna model for a single inverted vee dipole. At this early stage in the development process, I was interested in learning the basic characteristics of an inverted vee dipole so the simple model used in this first stage of simulations ignores the presence of both the second orthogonal dipole and the vertical mast in the near-field. Otherwise, the model is very similar to the geometry of the actual prototype antenna with each dipole arm extending down halfway to the ground from a height of 10 ft at a an angle of 45°. The apexes of the dipole arms are horizontally separated by a distance of 9 cm and connected by a straight wire with a wire port at its centre. Depending on the type of simulation, I either placed an alternating voltage source or an open-circuit load in the wire port at the antenna terminals. In transmit-mode simulations, the antenna is driven to radiate outwardly by an alternating voltage or current source at its terminals. In contrast, incident electromagnetic waves induce a voltage across the antenna terminals in receive-mode simulations. I used transmit-mode simulations to obtain the gain and impedance of the antenna while the effective length was obtained from a receive-mode simulation. The effective length ℓ is usually defined as

$$\ell = \frac{V_{\rm oc}}{E_i}, \tag{2.1}$$

where $V_{\rm oc}$ is the peak open-circuit voltage induced across the antenna terminals by an incident wave with a peak electric field magnitude of E_i (Stutzman & Thiele, 2012). For receive-mode simulations, I chose a plane wave of magnitude 1 V/m originating from the zenith and put a very large 1-GΩ resistive load between the antenna terminals, which effectively acts as an open-circuit. In this way, the effective length can be directly extracted from the receive-mode simulation as the voltage induced at the load.

The simulation results for the inverted vee dipole and the LWA antenna are compared in Figure 2.15. From the transmit-mode simulations, the gain and impedance magnitude of the inverted vee dipole are found to be consistently larger than those of the LWA antenna for frequencies $\lesssim 30$ MHz. From the receive-mode simulations, we see that, as expected, the effective length, and hence the voltage induced by an incident plane wave, is greater for the physically larger inverted vee dipole antenna. The beam solid angle Ω_A of each antenna is computed by numerically integrating over the normalized radiation pattern as a function of frequency.

$$\Omega_A(\nu) = \iint \frac{G(\theta,\phi,\nu)}{G_{\max}(\nu)} \sin\theta \; d\theta \; d\phi, \tag{2.2}$$

where $G(\theta,\phi,\nu)$ is the gain pattern in spherical coordinates (θ,ϕ) for every simulated frequency ν and $G_{\max}(\nu)$ is the maximum gain for every frequency, which serves to normalize the radiation pattern to 1.

2.4.2 Sky noise dominance of the prototype antenna

In this section, I establish a method for modelling the sky noise dominance of a simulated antenna system. The sky noise dominance is defined as the ratio of the sky noise power received by the antenna to the undesired noise power introduced by the FEE and the transmission line. It effectively describes the increase in integration time that is necessary to achieve the same signal output level as an ideal noiseless system (Erickson, 2003). For higher values of sky noise dominance, observations must contend with less system noise, which means that less integration time is required. Unlike other methods for determining the sky noise dominance (Ellingson, 2005), I propose a method that suits the case of an electrically small antenna with low radiation efficiency. I base my analysis on the sky noise-induced voltage at the antenna's load V_L as well as the total input-referred voltage noise $V_{n,\text{tot}}$ of the FEE amplifier. If we ignore the transmission line noise (it is small compared to the FEE noise), the sky noise dominance is given by

$$\gamma = \left(\frac{V_L}{V_{n,\text{tot}}}\right)^2. \tag{2.3}$$

The intensity of low-frequency radio emission from the Galactic poles is well fit by

$$I_\nu = I_g \nu^{-0.52} \frac{1-e^{-\tau(\nu)}}{\tau(\nu)} + I_{eg} \nu^{-0.80} e^{-\tau(\nu)}, \tag{2.4}$$

where $I_g = 2.48 \times 10^{-20}$ is the Galactic intensity constant, $I_{eg} = 1.06 \times 10^{-20}$ is the extragalactic intensity constant, and $\tau(\nu) = 5.0\nu^{-2.1}$ is the optical depth of free-free absorption (Cane, 1979). The frequency ν is in units of MHz, while I_ν is given in units of $\mathrm{W\,m^{-2}\,Hz^{-1}\,sr^{-1}}$. The Galactic

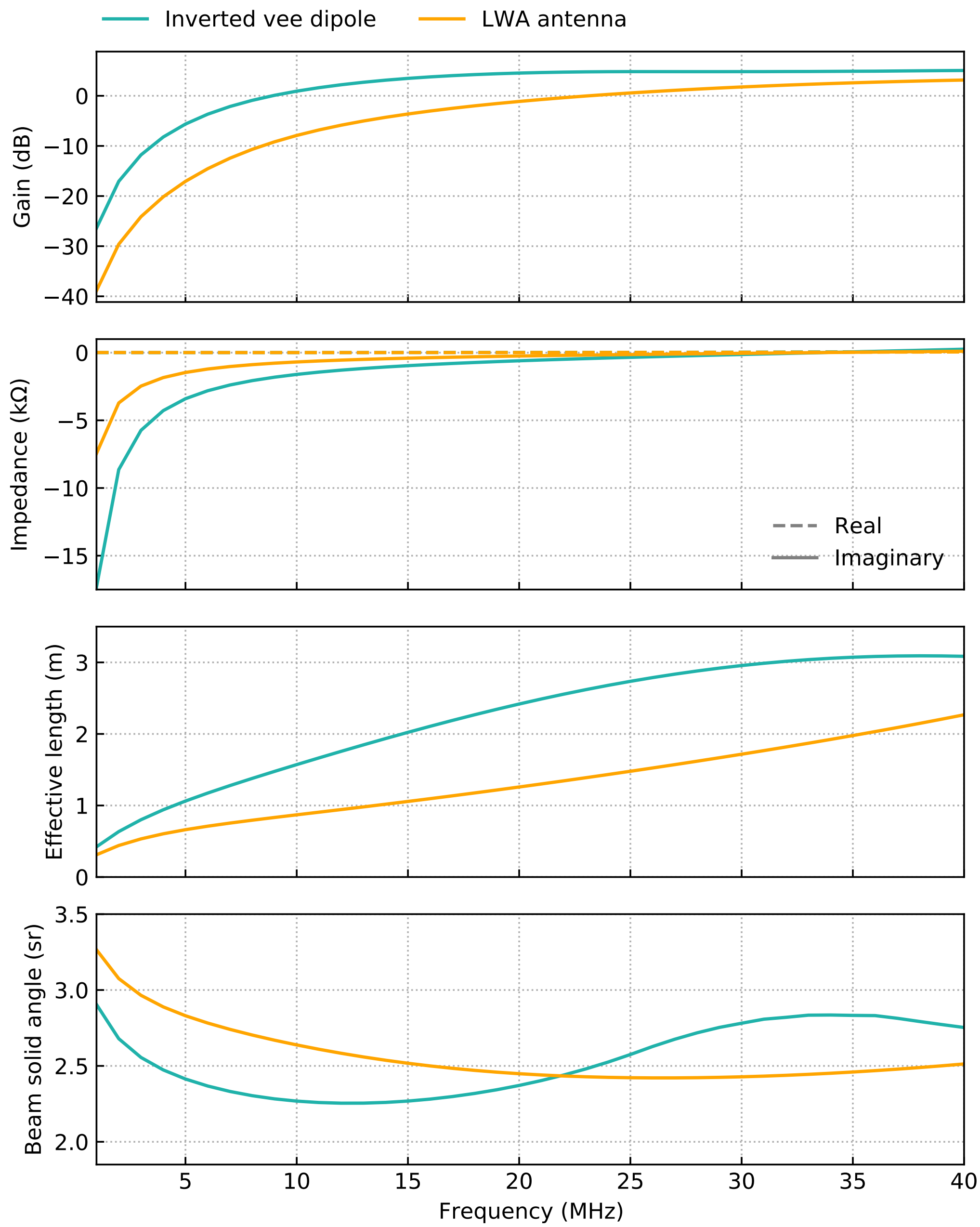

Figure 2.15: Results from transmit- and receive-mode simulations of an inverted vee dipole and the LWA antenna. The arms of the inverted vee dipole reach downwards at 45° from a height of 10 ft to a height of 5 ft above ground. The simulations are performed above "average" ground with a relative permeability of 13 and a conductivity of 0.005 S/m and no ground screen. The gain in the top panel is the maximum gain of the radiation pattern, which is in the zenith direction for nearly all plotted frequencies.

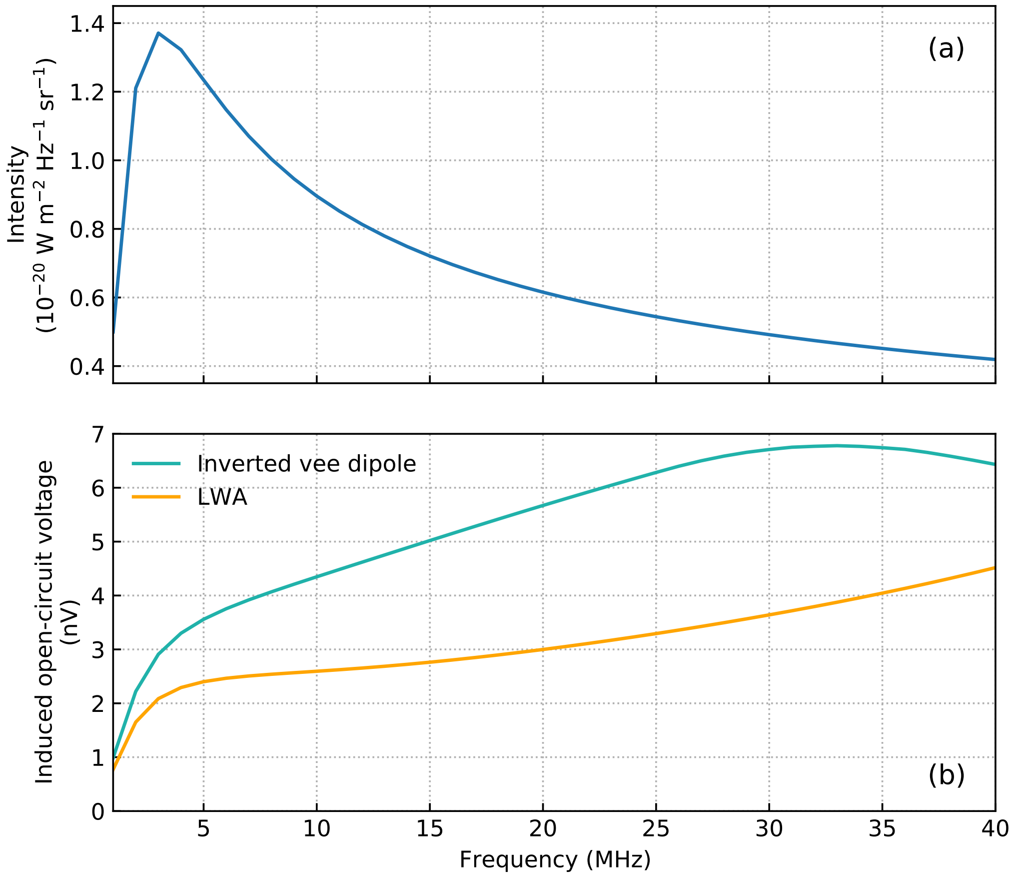

Figure 2.16: (a) Intensity spectrum of emission from the Galactic poles as modelled by Cane (1979). The turnover at $\sim 3\,\mathrm{MHz}$ is due to free-free absorption. **(b)** Open-circuit voltage induced at the antenna terminals by Galactic emission using the simulation results for the effective length of the inverted vee dipole and the LWA antenna.

intensity model given by Equation 2.4 is shown in Figure 2.16a. A voltage is induced at the antenna terminals by the Galactic noise and this voltage is related to the antenna's effective length via the electric field strength of the incident waves.

The incident intensity of Galactic noise can be converted to a spectral flux density S_ν seen by the antenna as follows:

$$S_\nu = \frac{1}{2}\int I_\nu d\Omega \approx \frac{1}{2} I_\nu \Omega_A, \tag{2.5}$$

where the factor of $1/2$ accounts for the linearly polarized dipole only being sensitive to half of the unpolarized sky noise power. The approximation holds if the Galactic intensity is assumed to be uniform over the entire sky, an unrealistic assumption that is nevertheless useful for estimating worst-case reception of Galactic noise. The spectral flux density of a plane wave is

$$S_\nu = \frac{1}{2}\frac{|E_i|^2}{\eta}, \tag{2.6}$$

where E_i is the peak magnitude of the plane wave's electric field and η is the impedance of free space. Treating Galactic emission as a plane wave, the electric field strength of the Galactic noise is obtained from the combination of Equations 2.5 and 2.6 into

$$E_i \approx \sqrt{I_\nu \Omega_A \eta}. \tag{2.7}$$

Thus, the Galactic emission described by Equation 2.4 induces an open-circuit voltage at the antenna terminals of

$$V_{\mathrm{oc}} = \ell \cdot E_i \approx \ell \sqrt{I_\nu \Omega_A \eta}. \tag{2.8}$$

A comparison of the induced open-circuit voltage for the inverted vee dipole and the LWA antenna is shown in Figure 2.16b. Evidently, the Galactic noise induces a higher voltage on the prototype inverted vee dipole than the LWA antenna, largely because of its greater effective length. The voltage transferred to the load from the induced open-circuit voltage can be calculated using the voltage divider formula:

$$V_L = \frac{V_{\mathrm{oc}}}{\sqrt{2}} \frac{Z_L}{Z_A + Z_L}, \tag{2.9}$$

where Z_L is the input impedance of the FEE, Z_A is the impedance of the antenna, and the factor of $\frac{1}{\sqrt{2}}$ gives V_L as a root-mean-square voltage value.

To continue, we must consider the circuit design of the high impedance FEE, which is currently being developed by Eamon Egan and Joëlle Bégin. It uses a non-inverting low-noise operational amplifier at each terminal for first-stage amplification of the received sky noise. Using the notation defined in the noise analysis diagram shown in Figure 2.17, the total input-referred voltage noise is

$$V_{n,\mathrm{tot}}^2 = V_n^2 + I_n^2 (Z_A \parallel R_T)^2 + I_n^2 (R_F \parallel R_G)^2 + 4kTR_T \left| \frac{Z_A}{Z_A + R_T} \right|^2 + 4kT(R_F \parallel R_G), \tag{2.10}$$

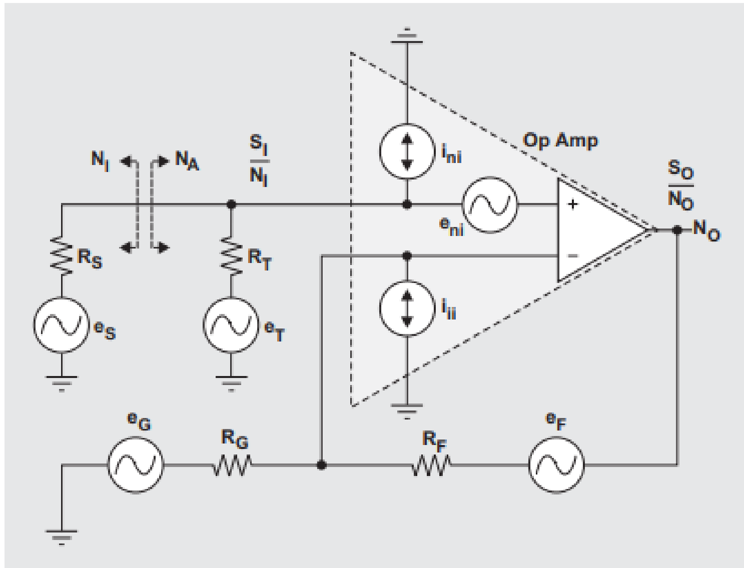

Figure 2.17: Non-inverting op-amp noise analysis diagram. Figure taken from Karki (2003).

where V_n is the voltage noise of the op-amp, I_n is the current noise of the op-amp, and $R_i \parallel R_j$ is the equivalent resistance to the parallel combination of R_i and R_j. The first term Equation 2.10 is the voltage noise of the op-amp, the second term is the current noise contribution through the non-inverting input, the third term is the current noise contribution through the inverting input, the fourth term is the thermal noise contribution of resistor R_T, and the last term is the thermal noise contribution of resistors R_F and R_G (Karki, 2003).

Finally, the sky noise dominance of the prototype inverted vee dipole was calculated for a variety of op-amps with different voltage and current noises. The included op-amps are the LT6202, LTC6228, and AD797 from Analog Devices as well as the LMH6626 and LMH6629 from Texas Instruments. The temperature was taken to be 298 K and the resistor values were set accordingly to an early version of the high impedance FEE circuit: $R_T = 100\,\mathrm{k\Omega}$, $R_F = 470\,\Omega$, and $R_G = 100\,\Omega$. The sky noise dominance was also calculated for the LWA antenna using the same set of parameters. Figures 2.18 and 2.19 show the sky noise dominance for both antennas. Relative to the LWA antenna, the inverted vee dipole displays an improved sky noise dominance above $\sim 12\,\mathrm{MHz}$, but there does not seem to be any improvement below this point. To achieve sky noise dominated observing at the lowest frequencies of interest, the next antenna prototype should be designed in a way to reduce the antenna's capacitive reactance, thereby increasing V_L and decreasing $V_{n,\mathrm{tot}}$ at low frequencies.

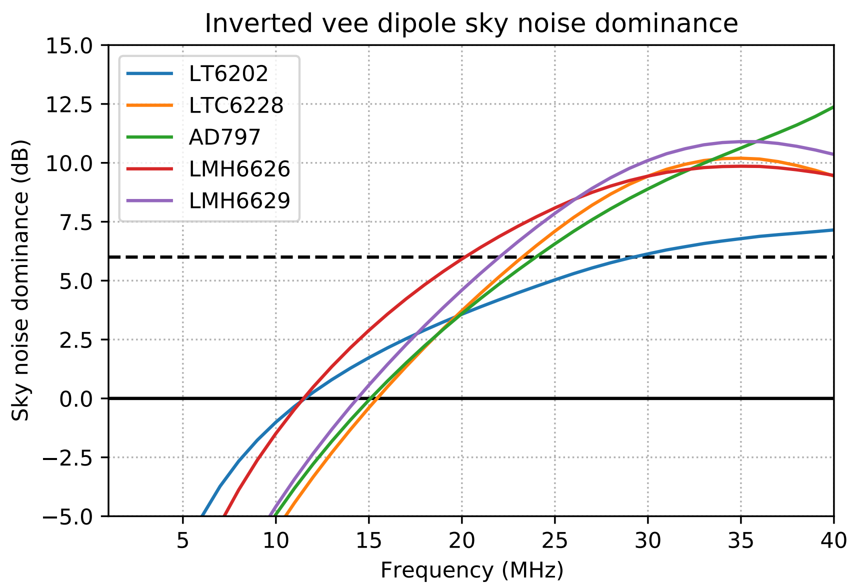

Figure 2.18: Sky noise dominance of the prototype inverted vee dipole with a high impedance FEE circuit. The sky noise dominance is plotted in dB for a selection of op-amps with different noise characteristics. The dashed line at 6 dB marks the sky noise dominance design criterion for the LWA within its operational frequency range of 20–80 MHz.

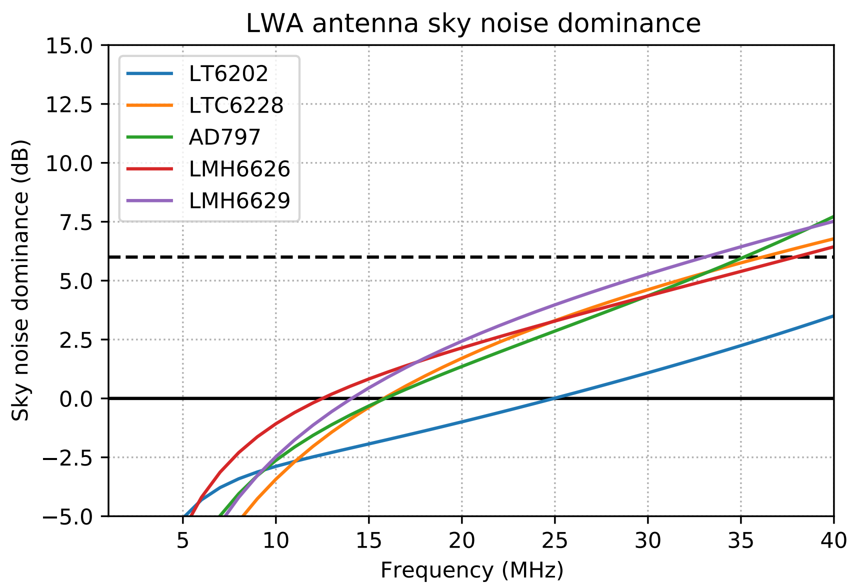

Figure 2.19: Sky noise dominance of the LWA antenna with a high impedance FEE circuit. The sky noise dominance is plotted in dB for a selection of op-amps with different noise characteristics. The dashed line at 6 dB marks the minimum sky noise dominance design criterion for the LWA within its operational frequency range of 20–80 MHz.

Chapter 3

RFI propagation mapping

In the search for suitable radio-quiet areas to install ALBATROS equipment, the desire for low RFI levels must be balanced against the accessibility of the site. For sites like Marion Island and MARS, where full ALBATROS arrays will be installed, the radio-quietness of the site is the most important consideration. However, such locations are burdened by limited accessibility and are not ideal for conducting short-term end-to-end system tests of radio astronomy instrumentation. These sorts of tests are essential for characterizing and improving the design and operation of the ALBATROS instrument. Full-system tests of radio-sensitive equipment also cannot be accomplished in standard lab environments as strong RFI overloads the antenna and preamplifier. Therefore, the identification of an auxiliary site where access is greater and RFI levels are moderately low is integral to the continued development of instrumentation for radio-sensitive experiments like ALBATROS. The motivation for the establishment of a nearby radio-quiet test site was further amplified by the COVID-19 pandemic and related worldwide travel restrictions. For ALBATROS, the global pandemic led to the cancellation of the 2020 voyage to Marion Island as well as the 2020 and 2021 deployments to MARS. As such, a local test site became critical for testing newly developed hardware in a radio-quiet environment.

At first glance, northern Québec has enviable characteristics for the establishment of a radio-quiet testing ground. The low population density in northern Québec points to the region having reduced RFI noise. Yet, many areas in the region are easily accessible from Montréal by car year-round because of the infrastructure that is maintained to support the operation of the province's extensive hydroelectric power generation network. Conversely, high-voltage power transmission lines, in this case originating from hydroelectric stations, are another source of strong RFI as they are susceptible to corona discharges and intermittent arcing. Nevertheless, some initial measurements of the RFI environment in the area around Matagami confirmed our suspicion that there are sites in northern Québec sufficiently radio-quiet and accessible for end-to-end testing of radio astronomy instrumentation.

The most accurate way of determining the quality of a location's RFI environment is with measurements, but measuring RFI levels across vast landscapes like northern Québec is costly and inefficient. For this reason, I produced maps that display the predicted propagation of RFI power from real transmitters based on parameters like the transmitter height, power, and frequency. The signal propagation model also considers the effect of irregular terrain features like mountains and valleys along the transmission path, which can help identify RFI shadows, areas that are naturally shielded from external RFI by their local geography. Using the power of a supercomputer, I extended the range of these computationally expensive RFI propagation maps to rapidly survey the expected RFI levels over large-scale areas at 30 m resolution. RFI in four areas of the Québec region, which were individually selected for their accessibility, local radio transmitter sparsity, and distance from high-voltage power lines, was surveyed in this manner in an effort to efficiently determine the most suitable location for a local radio astronomy test site.

3.1 Approach

The approach put forward to predict the quality of the RFI environment over large areas involves the use of the Longley-Rice model and many CPU cores. The Longley-Rice model is a well-known model for predicting the signal loss in transmitted radio signals propagating over irregular terrain (Longley & Rice, 1968). It was designed in the 1960s and is still widely used in many types of network coverage analyses. Today, many radio propagation software applications and open-source packages implementing the Longley-Rice model are available. The original source code in FORTRAN and C++ was also made available by the Institute for Telecommunication Sciences[1]. For this study, I chose to use `rasp`[2], a Python package implementing the Longley-Rice

[1] https://www.its.bldrdoc.gov/research-topics/radio-propagation-software/itm/itm.aspx
[2] https://gitlab.com/gnoble/rasp

model created by Gavin Noble, since its source code is readily accessible, its functionalities can be easily extended, large batch operations can be programmed efficiently, and the package is transferable between different operating systems. Another advantage of the `rasp` implementation of the Longley-Rice model is its speed, as its Python functions are compiled into optimized machine code that approaches C and FORTRAN speeds.

To accurately account for the attenuation caused by real terrain features between a given transmitter and receiver, the Longley-Rice point-to-point mode is used along with digital elevation data from the Shuttle Radar Topography Mission (SRTM; Farr et al., 2007). In the context of finding potential radio-quiet sites, the location of the receiver is unspecified, so I consider the signal propagation from a given transmitter to all other points in the region of interest. As the studied regions of interest are made larger in size, the point-to-point calculation of the predicted signal over the whole region becomes very slow. In this case, I was interested in surveying the propagation of RFI noise over vast areas encompassing tens of thousands of square kilometres and including thousands of transmitters. Therefore, I used GNU Parallel and a large number of CPU cores on the Niagara supercomputer[3] to break up the task. In this way, each CPU core was assigned the computation of the signal propagation for only one or two transmitters.

3.1.1 Longley-Rice model

The Longley-Rice model, which is also known as the ITS irregular terrain model, predicts the propagation of radio signals over irregular terrain between 20 MHz and 20GHz (Hufford et al., 1982). It is based on the fundamental mechanics of electromagnetic wave propagation and is intended for use over the wide parameter space given in Table 3.1. The model's predictions have been validated against measurements on numerous occasions (Lazaridis et al., 2013; Kasampalis et al., 2013, 2015), showing reasonable accuracy for the purposes of this work.

The Longley-Rice model can be operated in two modes: an area prediction mode and a point-to-point prediction mode. The point-to-point mode requires precise knowledge of the terrain while the area prediction modes relies on estimations of the area's general topography. Since detailed elevation data for most of the world is easily available, the point-to-point mode of the Longley-Rice model is most useful. There are three types of input parameters required by the point-to-point

[3] https://www.scinethpc.ca/niagara/

Table 3.1: Intended parameter space of the Longley-Rice model

Parameter	Range
Frequency (MHz)	20–20 000
Antenna heights (m)	0.5–3000
Distance (km)	1–2000
Surface refractivity (N-units)	250–400

model: antenna parameters, environmental parameters, and statistical parameters. The necessary antenna parameters are the transmission frequency, the great circle distance between the transmitter and the receiver, the effective heights of the transmitting and receiving antennas above ground, and the polarization, which can be either vertical of horizontal. The environmental parameters are the relative permittivity ε_r and conductivity σ of the ground, the surface refractivity N_s, and the climate. Typical values of $\varepsilon_r = 15$, $\sigma = 0.005\,\mathrm{S/m}$, and $N_s = 301$ N-units, which are associated with average conditions in a continental temperate climate, are assumed for all propagation predictions in this work. Finally, the statistical input parameters for the Longley-Rice model describe the variability of the received signal in time, location, and situation. The intended use of these last parameters is to express the percentage of time, locations, and situations in which a given mobile communications link budget would suffice. The statistical parameters are not as meaningful in the context of radio astronomy, so propagation losses of a statistical nature are generally ignored in this case.

As seen in Figure 3.1, there are three regimes of radio propagation considered in the Longley-Rice model. The first regime, which occurs in the common line-of-sight between the transmitter and receiver, is modelled by free space path loss and two-ray optics to quantify reflections. As a radio ray travels through the atmosphere, it is bent according to the surface refractivity. Just beyond the horizon, diffraction becomes important to the propagation of radio signal. In the Longley-Rice model, propagation in this diffraction-dominated zone is based on knife-edge diffraction theory. The electrical characteristics of the ground, its permittivity and conductivity, impact radio propagation in both the line-of-sight and diffraction-dominated regimes. At the furthest distances, forward scattering becomes the dominant propagation mechanism. An example of Longley-Rice signal propagation from a FM radio station over real terrain data is shown in Figure 3.2.

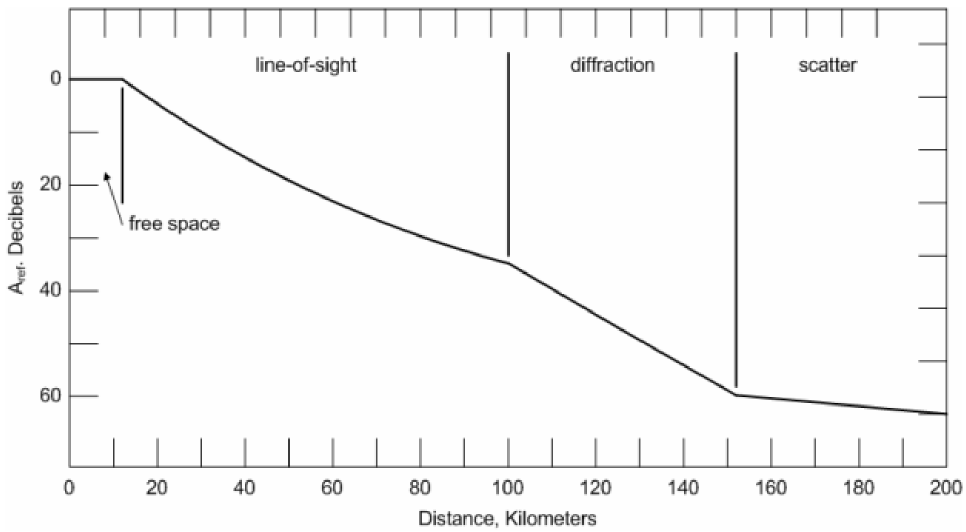

Figure 3.1: Typical signal attenuation compared to free space loss as a function of distance. Three distinct regimes of signal propagation are visible. Figure taken from Hufford et al. (1982).

The propagation of shortwave radio transmissions at frequencies below 20 MHz are difficult to model due to long propagation distances and high ionospheric variability at these low frequencies. Although frequencies $\lesssim 20$ MHz are well within the targeted frequency range of ALBATROS, the topography of a site will not greatly affect the amount of received low-frequency RFI. Thus, the propagation of RFI within the intended operation range of the Longley-Rice model is sufficient for determining a suitable radio-quiet test site for ALBATROS.

3.1.2 Workflow and implementation

As noted, this analysis uses the `rasp` implementation of the Longley-Rice model in combination with GNU Parallel on the Niagara supercomputer to reduce computing time. Before any propagation calculations, the first step is obtaining and parsing a transmitter database for the chosen region. Often governmental institutions keep publicly accessible databases containing useful information on registered transmitters in their jurisdictions. In this case, I used the Spectrum Management System database[4] from the Government of Canada. It contains information relating to all registered transmitters in the country. Examples of unregistered transmitters that are left out of this database and therefore not included in the following analysis are most amateur radio antennas and

[4] http://sms-sgs.ic.gc.ca/eic/site/sms-sgs-prod.nsf/eng/h_00010.html

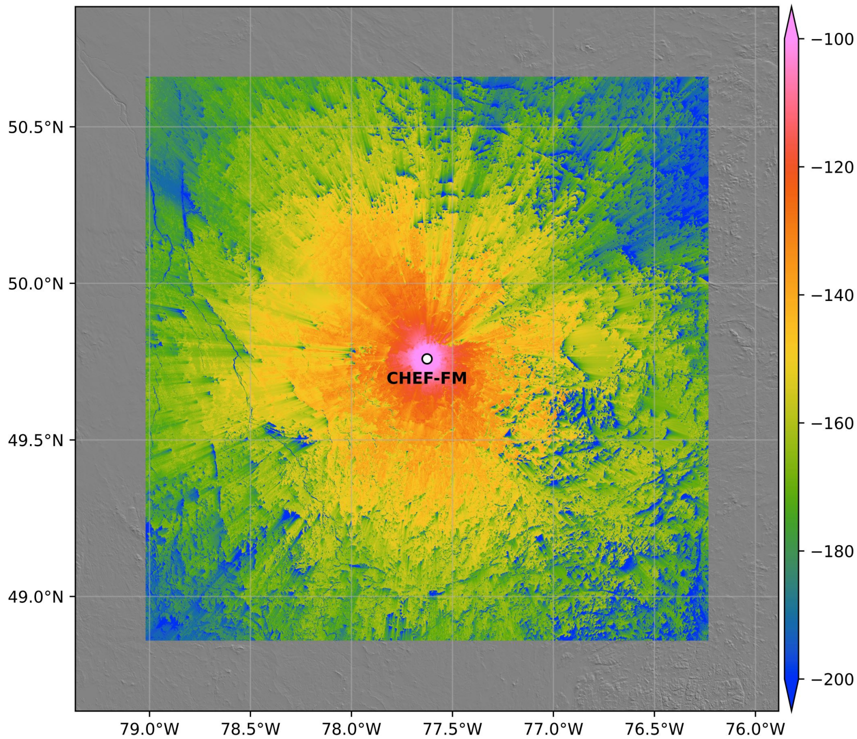

Figure 3.2: Propagated power from the CHEF-FM 99.9 MHz radio station in Matagami, Québec. The effective radiated power of the broadcasting antenna is 15.6 dB and its height is 17 m. The radiation patterns of both the transmitting and receiving antennas are assumed to be isotropic. The color scale is the power received by an antenna at a height of 1.5 m. The greyscale background shows the gradient of the SRTM elevation data over an area of 250×250 km. The size of the region within which the propagation was calculated is 200×200 km.

citizens band radio. Unfortunately, it is generally difficult to obtain the radiation pattern data for any significant number of transmitters, so the transmitters in this analysis were assumed to be radiate isotropically. At this time, I also gathered information relating to the Québec power network and road infrastructure from the Ministery of Energy and Natural Resources' topographic maps[5] and transportation network database[6], respectively. The elevation data is pulled from the global SRTM 1-arcsecond database (Jarvis et al., 2007). Then, promising areas can be identified by examining the gathered databases for areas with low transmitter density, road access, and a lack of power transmission lines. The elevation database can also be surveyed for large mountain ranges

[5] https://mern.gouv.qc.ca/repertoire-geographique/cartes-topographiques-echelle-1-100000/
[6] https://mern.gouv.qc.ca/repertoire-geographique/adresses-quebec-reseaux-transport/

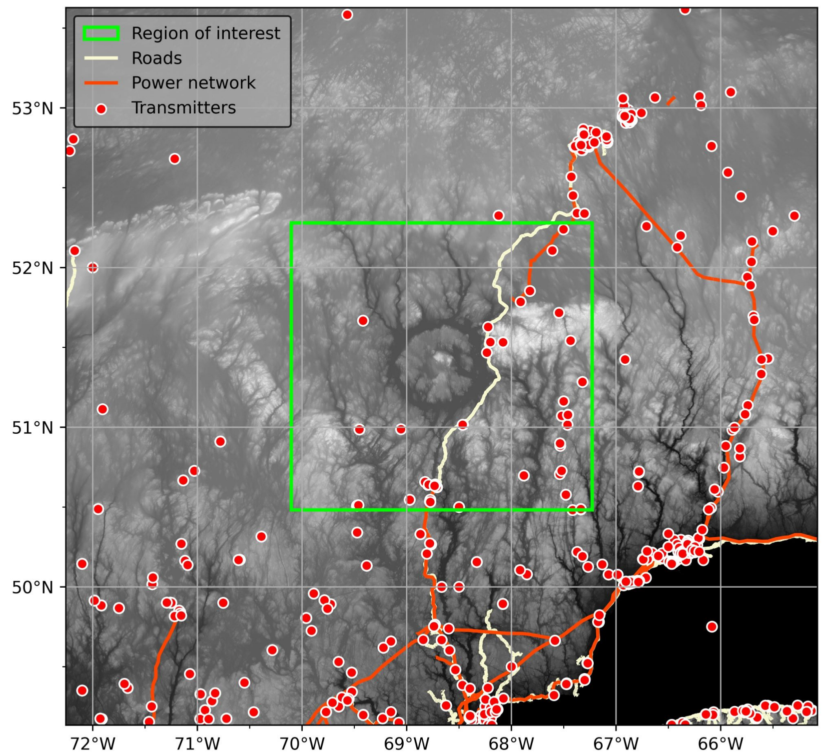

Figure 3.3: Sample area selected for study. The region of interest is centred on the Manicouagan reservoir, where there is road access, no nearby power transmission lines, and few radio transmitters within the range of 20–300 MHz. The wider area shown here is the inclusion area for transmitters in the propagation calculations of the specified region of interest.

and valleys. An example of a promising radio-quiet area identified in this manner is depicted in Figure 3.3. A region of interest within which signal propagation calculations will be made must be specified as well as a larger bounding box from which to sample transmitters. Indeed, RFI power can propagate into the region of interest from outside sources. In the example, the region of interest is a 200×200 km area outlined in green around the Manicouagan reservoir. The transmitters included in the propagation calculation, marked in red, are sampled from a larger area that is 500×500 km in size. There are a total of 3432 transmitters included in this example case between 20–300 MHz.

Once the databases have been prepared, the Longley-Rice propagation calculations for each transmitter can be run on the supercomputer. As the computation of the propagation from each transmitter is an independent process, they can be separated onto different CPU cores with the results saved individually to reduce computing time. The separation is accomplished using GNU Parallel, which is specifically designed for this type of situation, and each CPU core is assigned two transmitters (one for each hyperthread). Each node of the Niagara cluster has 40 cores (80 hyperthreads) and there are 2024 nodes in the cluster. Therefore, each node processes the propagation calculations for 80 transmitters. If there are enough available nodes, these calculations can all be accomplished simultaneously, thereby eliminating the time cost associated with the number of transmitters that would otherwise be processed sequentially. However, the computing time that is now mainly dependent on the size of the region of interest can still become problematic for extremely large-scale surveys. For the sample area given in Figure 3.3, the total computing time was 2 h 27 min using 43 nodes. The mean time spent computing on a node was 2 h 14 min for a total of $\sim$ 3800 core-hours.

Finally, the propagated power from each individual transmitter inside the defined inclusion zone and desired frequency window is combined in a linear sum. In this way, the total RFI power received at any location in the region of interest is mapped. The RFI power from each transmitter is weighted equally meaning that the resulting map does not account for the duty cycles of different transmitters. As such, the RFI power map gives a worst-case analysis for the RFI environment at any site. On-site measurements may notice that seemingly noisy sites in these maps are actually quiet in reality because a nearby radio transmitter is never used.

3.2 RFI maps at potential radio-quiet sites

The locations of all registered transmitters, roads, and high-voltage power transmission lines in the province of Québec are displayed in Figure 3.4. This map also shows the locations of the four areas that were studied in this RFI propagation analysis: the Algonquin Radio Observatory, La Vérendrye wildlife reserve, the area around Matagami, Québec, and the Manicouagan reservoir.

The assembled RFI propagation maps illustrate the cumulative power from all registered transmitters in the defined inclusion zone and within the frequency window spanning 20–140 MHz, that is relevant to ALBATROS. Other maps were also created that extend up to 300 MHz. In all cases, the height of the receiving antenna is assumed to be 3 m above ground while the transmitter height, if unlisted in the database, is assumed to be 10 m. All other input parameters for the antennas

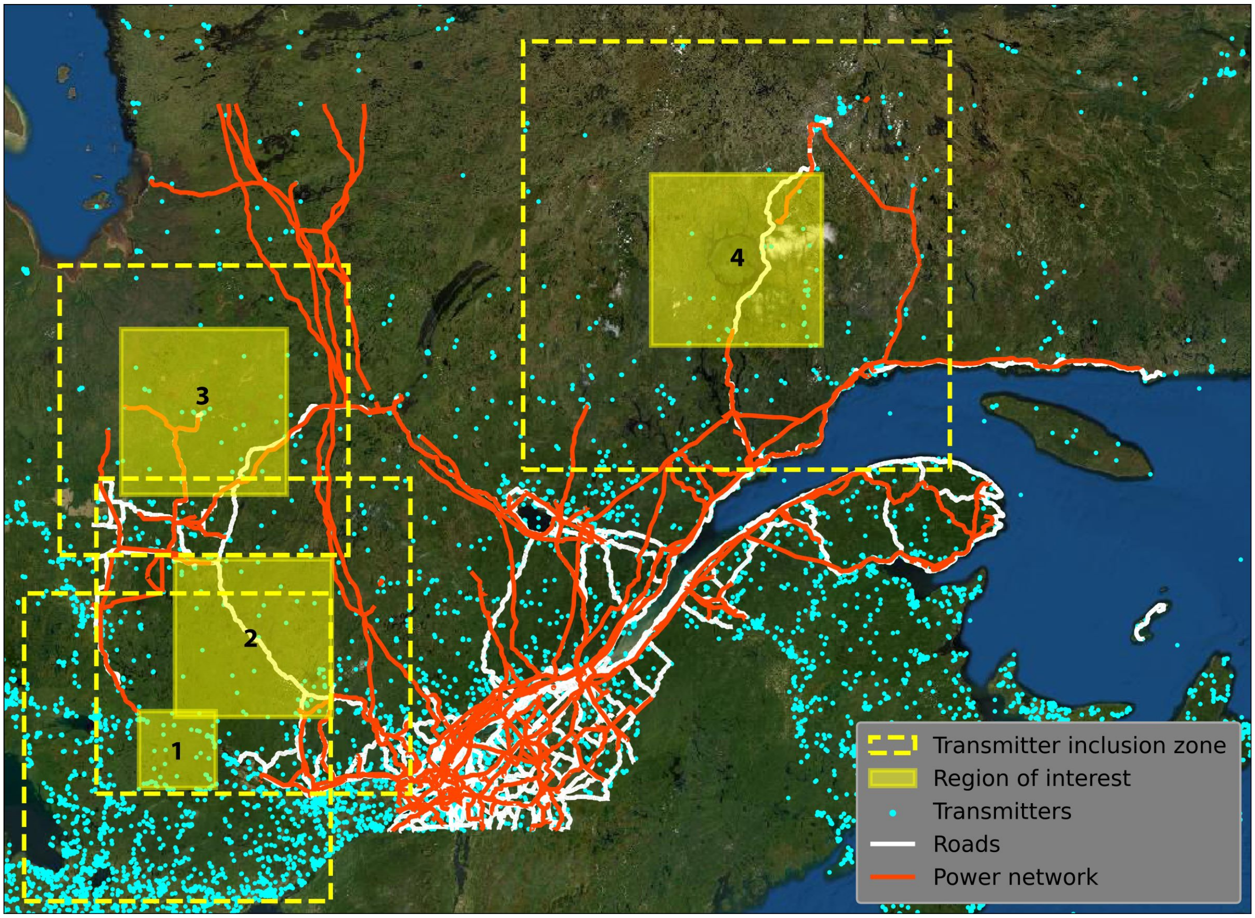

Figure 3.4: Transmitters, roads, and power transmission lines in the Québec region. The identified potential radio-quiet areas are (1) the Algonquin Radio Observatory, (2) La Vérendrye wildlife reserve, (3) Matagami, Québec, and (4) the Manicouagan reservoir. Only road and power infrastructure in the province of Québec are displayed. The power network is also cut off at the 53$^{\text{rd}}$ parallel, but in reality extends further north.

were consistently listed in the used database. The colour scale is identical in all following RFI propagation maps.

3.2.1 Algonquin Radio Observatory

The Algonquin Radio Observatory is an established site for radio astronomy that is located less than 400 km west of Montréal. It is situated in a geographical depression that provides moderate RFI shadowing. The mapped region of interest is smaller than the others at only 100×100 km in size because the observatory occupies a precise site and the amount of transmitters in the

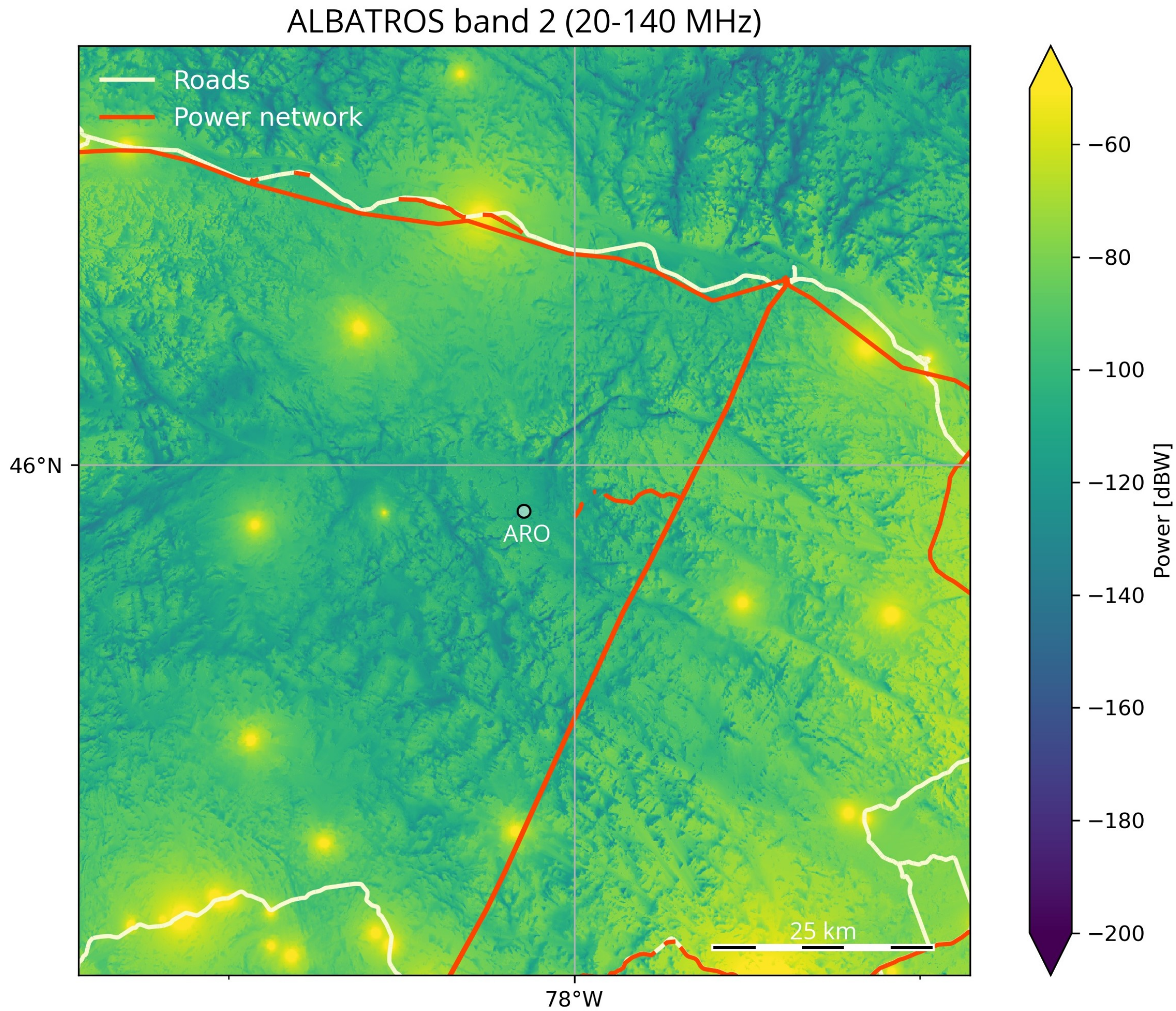

Figure 3.5: Cumulative RFI power map for the region surrounding the Algonquin Radio Observatory (denoted as ARO), including regional roads and high-voltage power transmission lines.

400×400 km inclusion zone is extremely large. There are over 11,000 registered transmitters in this space, including many FM broadcast stations. The RFI power map of the Algonquin Radio Observatory, shown in Figure 3.5, was produced as a comparison point about which to assess the quality of other sites.

3.2.2 La Vérendrye

La Vérendrye is a wildlife reserve situated less than 400 km north-west of Montréal. The specified region of interest is 200×200 km in size and the transmitter inclusion zone covers an area of

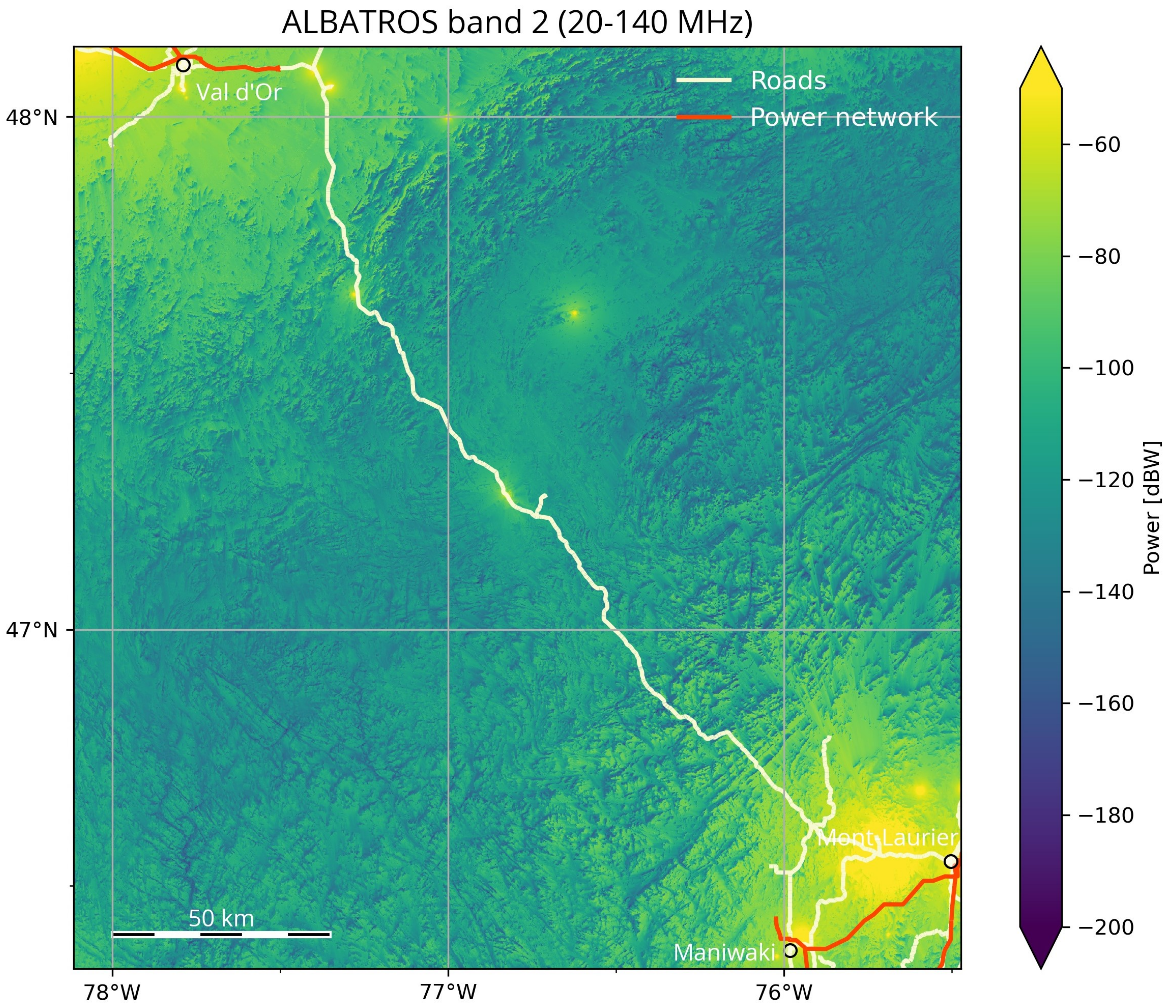

Figure 3.6: Cumulative RFI power map for the region surrounding the La Vérendrye wildlife reserve, including regional roads and high-voltage power transmission lines.

400×400 km. Approximately 6700 transmitters are encompassed in this area, of which only a small fraction are near the wildlife reserve itself. The only power transmission lines in the region of interest are near its extremeties and a road provides access through the middle of the region. The RFI map for La Vérendrye is shown in Figure 3.6.

3.2.3 Matagami

Matagami is a small town in northern Québec located approximately 560 km north-west of Montréal. The region of interest covers a 200×200 km, while the transmitter inclusion zone outlines

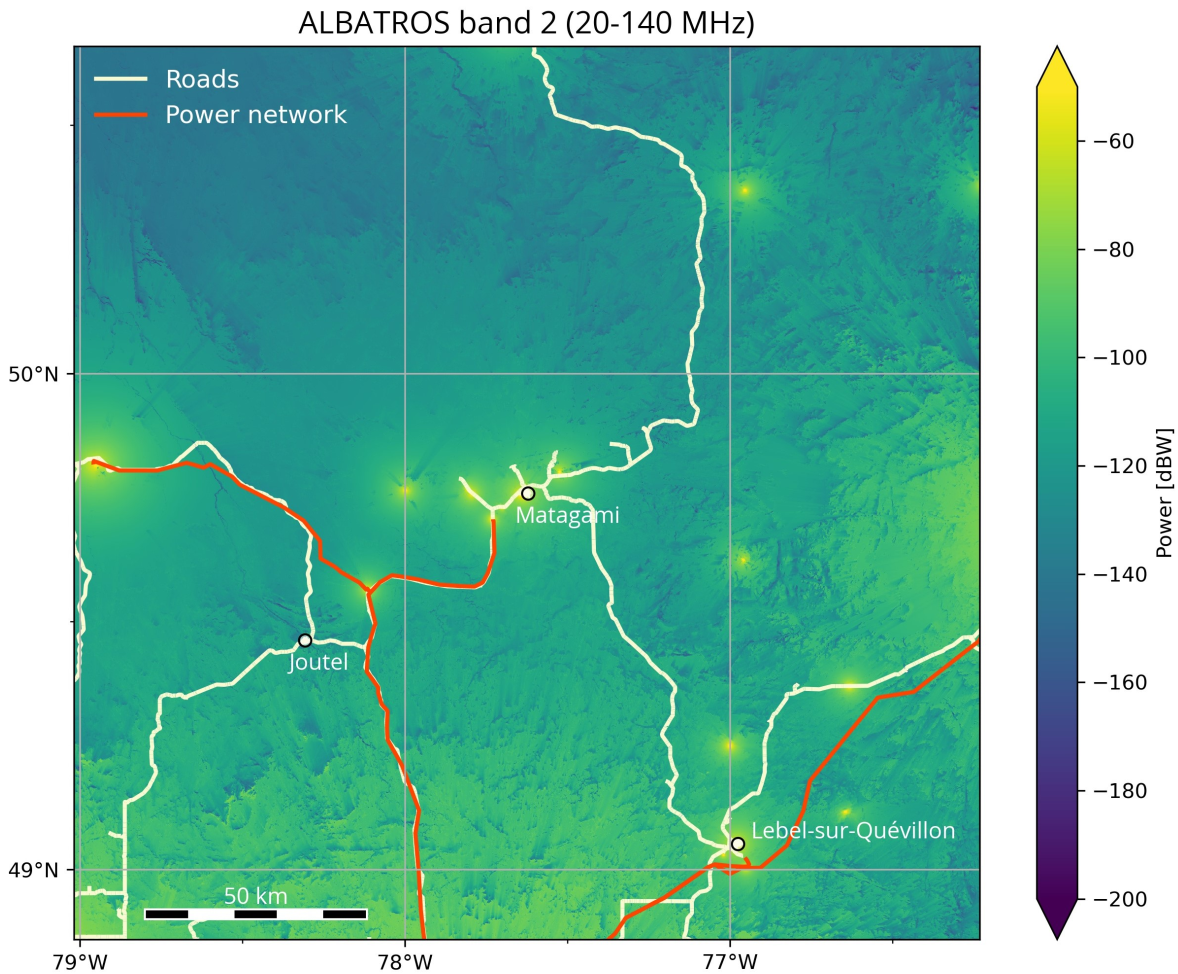

Figure 3.7: Cumulative RFI power map for the region surrounding Matagami, Québec, including regional roads and high-voltage power transmission lines.

a 350×350 km area that includes approximately 1700 transmitters. The RFI power map for the Matagami area is shown in Figure 3.7, where power lines can be seen to the south of the town and a road leading north from the town allows access to potential radio-quiet test sites.

3.2.4 Manicouagan

The Manicouagan reservoir is a distinctly annular lake that is sometimes referred to as the Eye of Québec. It is located approximately 800 km north of Montréal. The reservoir was flooded by the construction of hydroelectric dams (Manic-1, Manic-2, Manic-3, and Manic-5) downstream. Manic-5 and Hart-Jaune are the two closest hydroelectric power generation stations. Uapishka

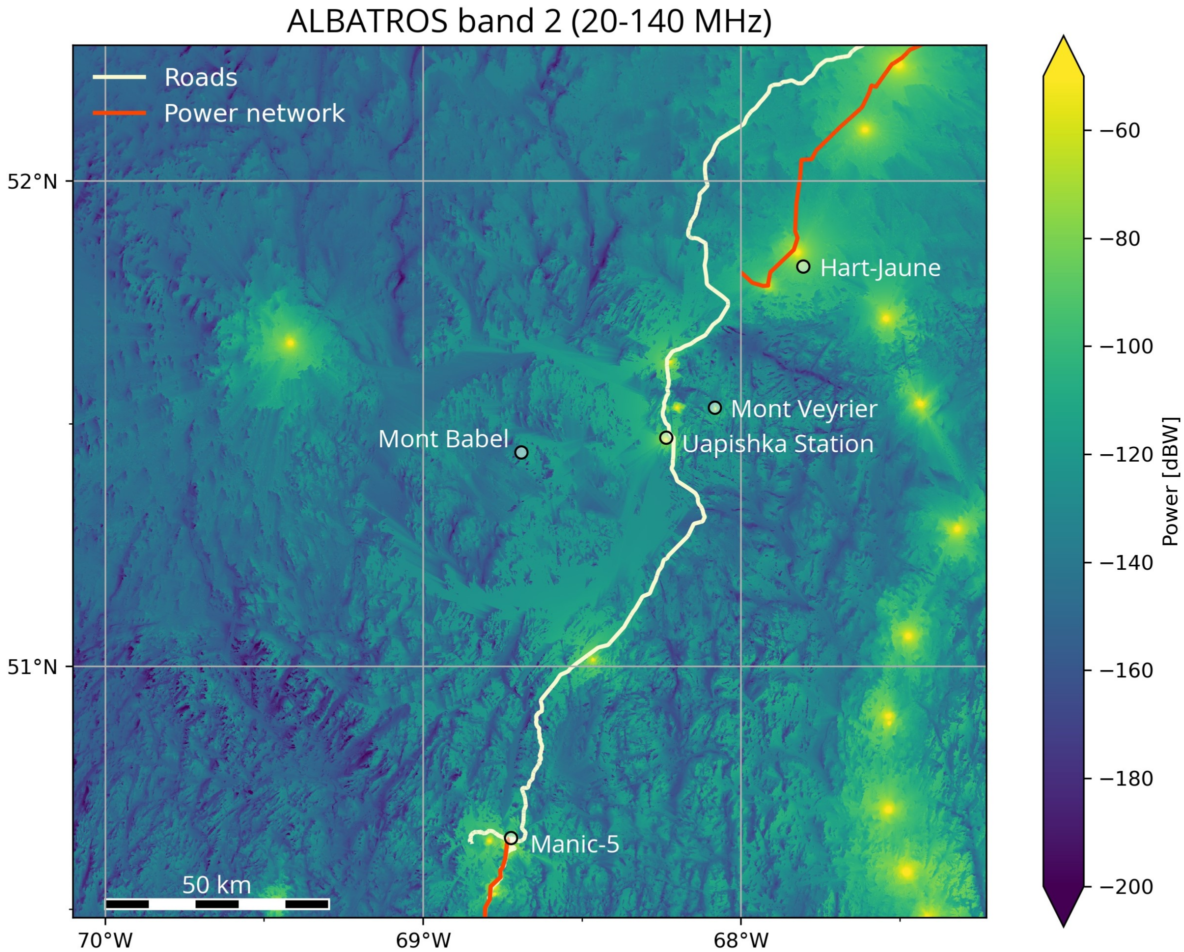

Figure 3.8: Cumulative RFI power map for the region surrounding the Manicouagan reservoir, including regional roads and high-voltage power transmission lines.

Station is located on the eastern shore of the reservoir. The region of interest computed for this area is 200×200 km, while the transmitter inclusion zone is 500×500 km and includes around 3400 transmitters. A road travels the eastern edge of the reservoir, along which there are no power lines for an extended stretch.

3.2.5 Comparison between potential sites

By visually comparing the RFI propagation maps above, the Manicouagan reservoir appears to be generally more radio-quiet than the other discussed sites. The contrast is especially stark when comparing the map of the Manicouagan reservoir to that of the Algonquin Radio Observatory, an

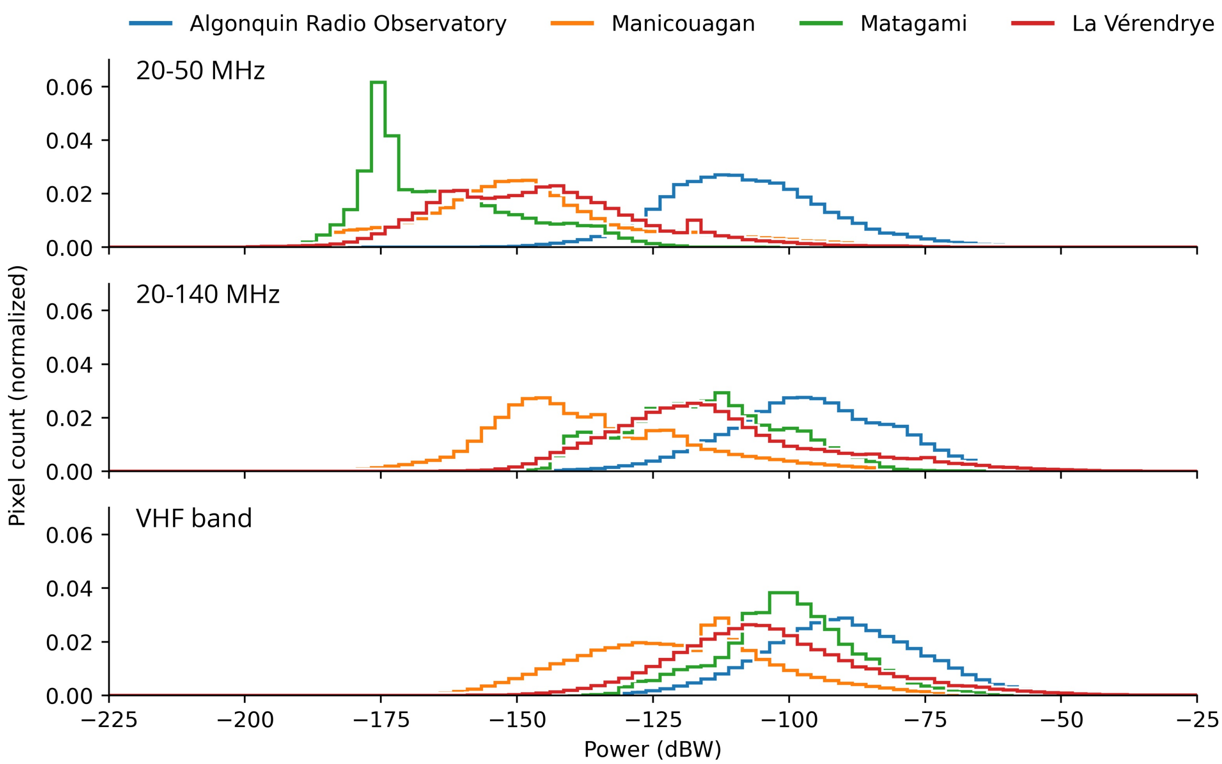

Figure 3.9: Histogram comparison of the cumulative RFI power level across all analyzed regions in three different frequency windows.

established radio astronomy site. Additionally, there appears to be a well-shielded RFI shadow in the river valley immediately north of Mont Veyrier. A quantitative comparison of the cumulative RFI power propagated within each defined region is portrayed in Figure 3.9 for three different frequency windows. The lowest frequency window of 20–50 MHz is useful for understanding the impact of RFI sources at the low end of the VHF band, which is important for the targeted frequency range of ALBATROS. In general, there are fewer transmitters in this band and they are usually used for low-power land-mobile communications. From the Longley-Rice propagation predictions, the general area around Matagami is particularly radio-quiet at frequencies between 20–50 MHz. The second comparison considers the frequency range between 20–140 MHz, matching the entire operational frequency span of the ALBATROS experiment that is within the valid modelling range of the Longley-Rice model. This band includes FM broadcast frequencies, which can overload or otherwise interfere with the reception of Galactic signal at most sites. RFI levels in this band are expected to be lowest at Manicouagan, confirming the earlier visual conclusion. Over the entire

VHF band (30–300 MHz), Manicouagan is still found to be the quietest region. In all cases, the Algonquin Radio Observatory receives the highest RFI levels, whereas the Manicouagan reservoir region is predicted to have the quietest RFI environment in the VHF and 20–140 MHz bands and the second quietest RFI environment in the 20–50 MHz band. Evidently, northern Québec offers many benefits in terms of radio-quietness compared to an established radio astronomy site like the Algonquin Radio Observatory. Of the surveyed regions, the Manicouagan reservoir is expected to be the most favourable for the establishment of an accessible and moderately radio-quiet testing site.

Chapter 4

2021 Uapishka deployment

Uapishka Station is a research centre hosted on the eastern shore of the Manicouagan reservoir, in northern Québec. The Manicouagan reservoir was identified as one of the most radio-quiet areas that is easily accessible by road in the Québec region by the RFI propagation predictions presented in Chapter 3. The area is projected to be considerably more radio-quiet than even established sites for radio astronomy in the region like the Algonquin Radio Observatory. The accessibility of Uapishka is also a major advantage, especially when compared to Marion Island and MARS where access is difficult due to their remoteness. Instead, Uapishka Station is quieter than its regional comparables and accessible enough to feasibly allow regular visits for installation, maintenance, monitoring, and updating of on-site ALBATROS equipment throughout the year. Therefore, Uapishka was chosen as the grounds for field tests of newly developed ALBATROS hardware and software.

The first trip to Uapishka Station was in July–August 2021. During this time, a total of ten willing participants (including myself) spent up to three weeks each at Uapishka Station. The goals of this deployment were to assess the RFI quality of the area, determine a suitable location for antenna installations, install at least two independent antennas and back-end electronics enclosures, and test the robustness of the latest upgrades to the instrument. In this chapter, I will describe the antenna installations that were made at Uapishka and demonstrate the RFI quality of the site. I will also present preliminary results from the first-ever correlation of two autonomously-operating ALBATROS elements.

4.1 Antenna installations

Approximately 800 m south of the main station is a large open space where we were granted permission to install our scientific equipment. The site is next to the abandoned buildings of an old compound and there are several camping sites within 200 m of the antennas. In total, three LWA antennas and a control hub were installed at this site along with one prototype dual-polarization inverted vee dipole that was set up temporarily. The antennas were arranged as depicted in Figure 4.1 and they were orientated such that one polarization of each antenna is aligned with geographic north. A pair of 30-m coaxial cables links the two closest LWA antennas (LWA-N and LWA-S) to the control hub, where the hybrid solar-methanol power system is located. During this deployment to Uapishka, we had two back-end electronics enclosures and could therefore independently operate up to two dual-polarization antennas at a time. However, only the two LWA antennas linked to the control hub could be powered by the automatic methanol-solar power system. The power supply for all other antennas relied on manually charged 12-V batteries.

The separation between the LWA-N and LWA-S antennas is constrained by the length of the coaxial cables connecting them to the control hub, so the total distance between these two antennas is ~ 55 m. The east-west baseline between LWA-N and LWA-S is ~ 25 m, which is the maximum allowed by the terrain of the site. The LWA-E antenna was installed ~ 65 m north-east of the control hub. The longest obtainable east-west baseline for the arrangement of antennas shown in Figure 4.1 is ~ 65 m, between LWA-N and LWA-E.

4.2 RFI environment

Upon arrival at Uapishka, we set out to characterize the area's RFI environment. Rapid RFI surveys were conducted at various nearby sites using a D130J Super Discone Antenna and the spectrum analyzer function on a FieldFox N9914A, both of which are easily portable. Near the main base, solar panels generated noticeable levels of broadband RFI, but beyond the building's immediate vicinity, RFI levels were found to be reasonably low.

In Figure 4.2, a representative sample of waterfall plots from the LWA-N and LWA-S antennas demonstrate the quality of the RFI environment at Uapishka. The outputs from the north-aligned

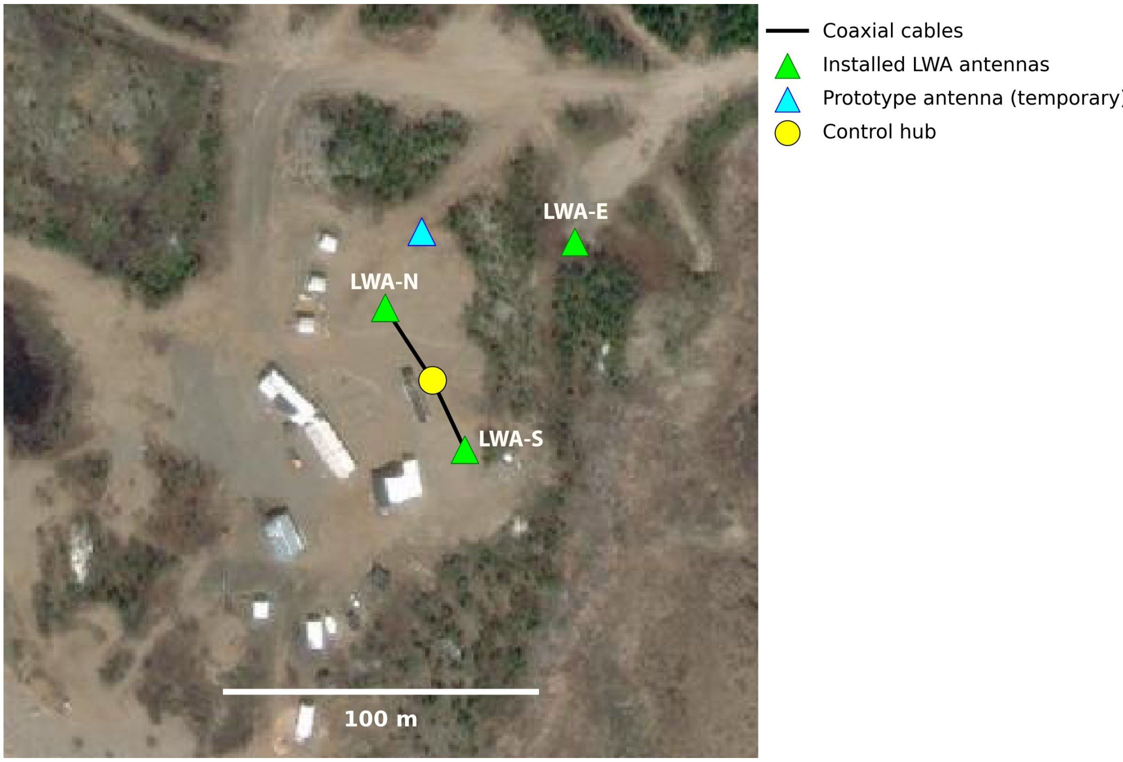

Figure 4.1: Satellite imagery of the antenna installation site near Uapishka Station. The locations of the antennas are marked on the map along with the location of the control hub. The structures visible to the south and west of the antenna installations are abandoned buildings from an old base. Some of these structures no longer exist. The displayed site is ~ 800 m south of the main building for Uapishka Station.

polarization of each antenna were directly-correlated by the SNAP board's FPGA. These sample measurements were taken on July 30–31 2021 over a total of nearly 20 hours and exemplify fairly typical daytime and night-time RFI conditions during the summer at Uapishka. ORBCOMM signals are easily discernible at ~ 113 MHz, aliased down from ~ 137 MHz. The strongest and most consistent source of RFI is shortwave radio at $\lesssim 20$ MHz. Shortwave radio propagates around the world via reflections in the ionosphere, which are possible up to a maximum frequency ~ 3 times higher than the plasma cutoff frequency. At night, the plasma cutoff frequency subsides, allowing clear views of the Galaxy down to lower frequencies. However, these observations were taken while the Perseid meteor shower was ongoing, causing RFI from the television and FM bands (44–88 MHz and 88–108 MHz, respectively) to appear more frequently than usual due to scattering off ionized meteor trails. Despite the suboptimal observing conditions, RFI from FM stations is generally faint and intermittent while television stations are only seen on rare occasions. As qualitatively evidenced by the waterfall plots, the RFI environment at Uapishka is suitably radio-quiet for end-to-end system tests of radio-sensitive instrumentation. A more quantitative calculation of the RFI occupancy rate is currently underway. Lower levels and occurrence rates of RFI are expected during the winter when there is less human activity at Uapishka Station, especially at the nearby campgrounds.

For these measurements, the solar panels at the control hub were switched off to reduce self-generated RFI from the solar charge controller when it is operational during the day. In the future, self-generated RFI from the solar charge controller will be mitigated with filtering techniques that were successfully tested with the solar-powered ALBATROS station on Marion Island. The RFI generated by the EFOY methanol fuel cell will also need to be carefully investigated. Indeed, a sample of the results from conducted voltage emission tests conducted by the manufacturer is shown in Figure 4.3 and suggests that faint RFI features at intervals of $\sim 230\,\mathrm{kHz}$ may emanate from the EFOY Pro 2400 methanol fuel cell.

4.3 Correlation of a two-element autonomous interferometer

Many configurations of two- and three-element interferometers were attempted using the three LWA antennas, two back-end electronics enclosures, and one automatic methanol-solar power system on hand at Uapishka. In this section, I will describe and present preliminary results from the correlation of two autonomous LWA antennas using a small frequency window of baseband data between $\sim$ 40–44 MHz and 4-bit quantization. Recording baseband at 4-bits allows the autospectrum magnitude to be recovered in post-processing, which is useful for comparison against the directly-computed spectra. Only small bandwidths can be saved to baseband data and the chosen frequency window coincides with the peak in the response of the LWA antenna.

The setup illustrated in Figure 4.4 was used to record baseband data from the LWA-N and LWA-S antennas on separate back-ends, each containing independent clocks. The outputs of the north-aligned polarizations of LWA-N and LWA-S were passed to the first input of each SNAP board. Additionally, the north-aligned polarization of LWA-N was also passed to the second input on one of the SNAP boards, so that the offline correlation result can be verified against the directly-

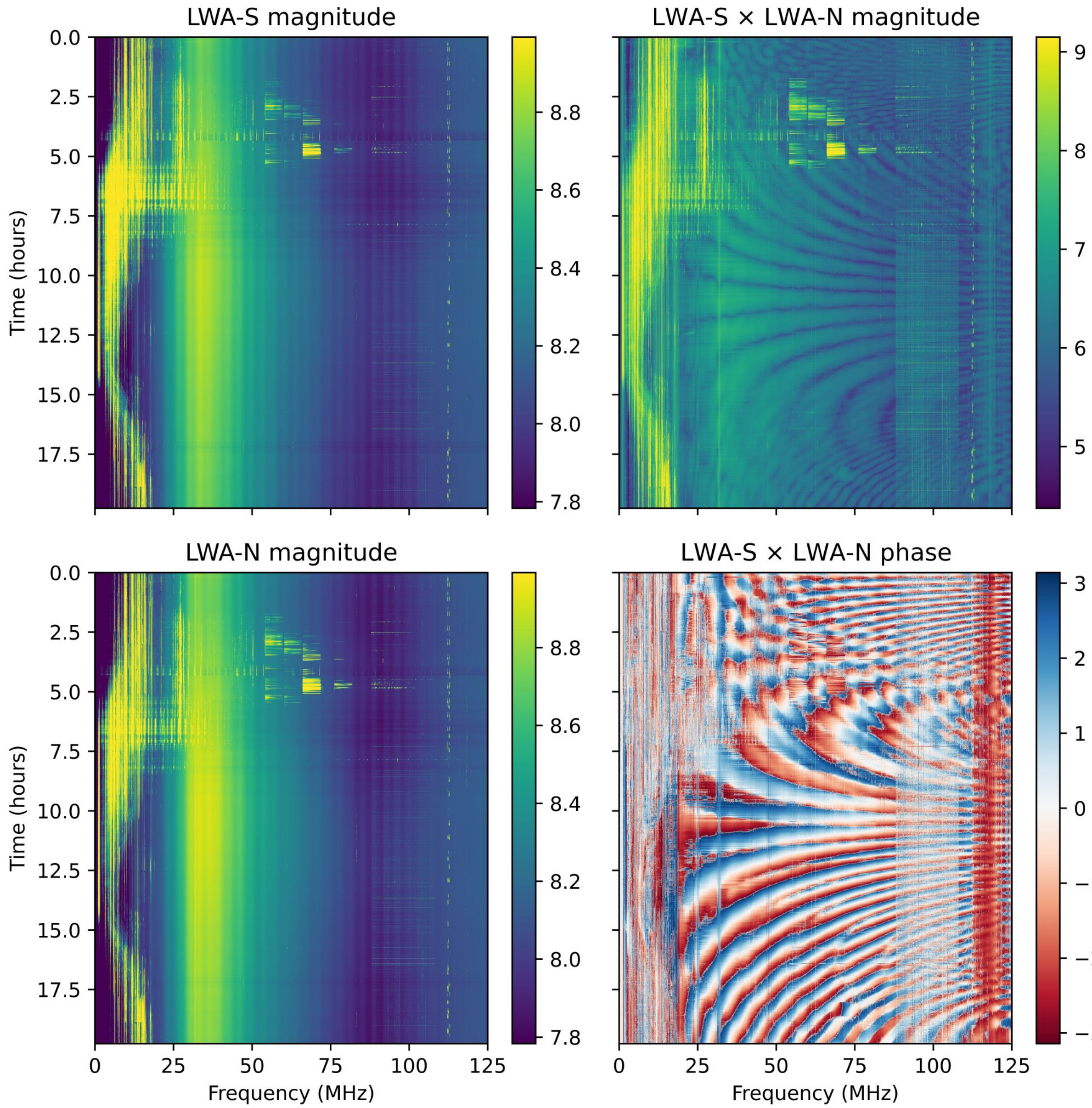

Figure 4.2: Directly-computed auto- and cross-spectra from co-aligned polarizations of the LWA-N and LWA-S antennas. Auto-spectra magnitudes are on the left while the cross-spectrum magnitude and phase are on the right. The colour scale for the magnitudes is in uncalibrated logarithmic units and the phase is given in radians. The waterfall plots begin at approximately 14:30 EDT on July 30 2021 and end around 10:15 EDT on July 31. Fringes from the Galaxy passing over the two-element interferometer are present in the cross-spectrum for the daytime and night-time data, yet the fringes are most prominent at night.

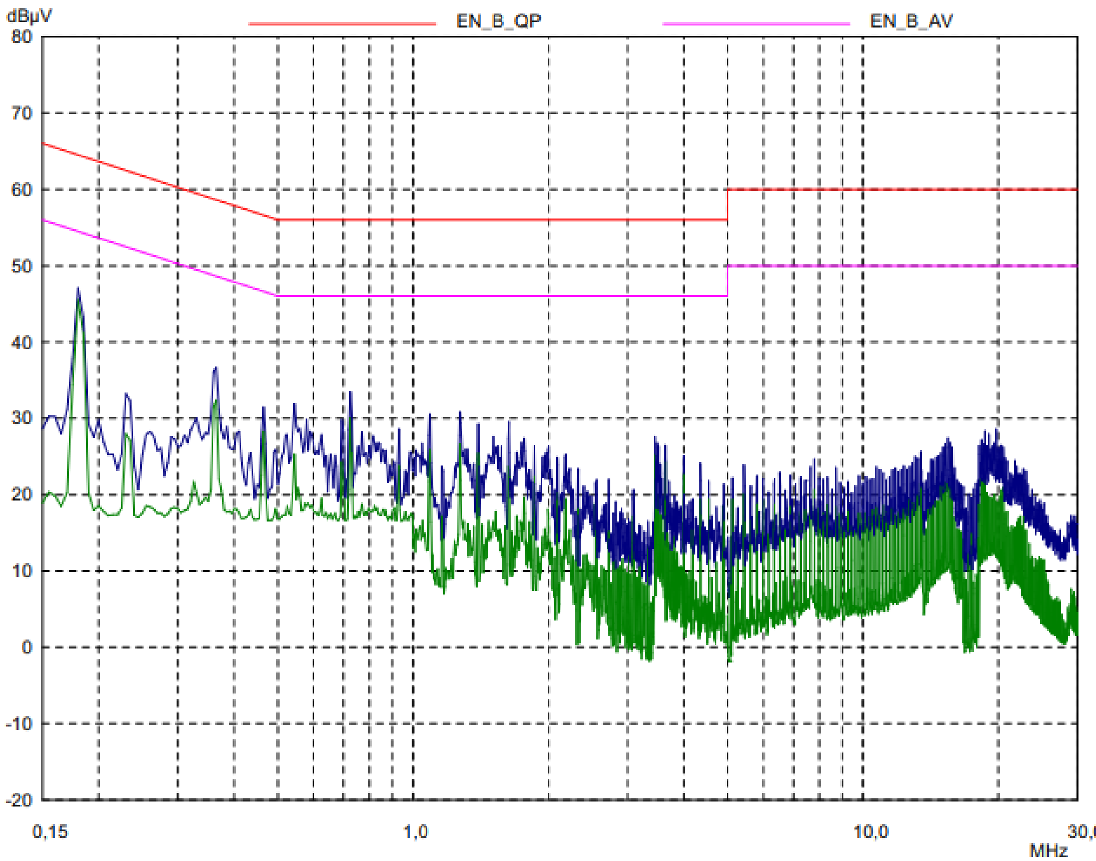

Figure 4.3: Conducted voltage emission test results for the EFOY Pro 2400 Duo methanol fuel cell in its 24 V configuration. A repeated feature is seen throughout the tested bandwidth at constant intervals of ~ 230 kHz. The green line represents the averaged spectrum measurement while the blue line represents the peak spectrum. The red and pink lines give maximum emission limits to meet electromagnetic interference industry standards. Both the 24 V line and the ground line demonstrate identical behaviour. Figure taken from an electromagnetic compatibility report made by Schwille Elektronik for the manufacturer.

computed cross-spectrum. The measurements discussed here were taken overnight on July 26–27 2021. Power was supplied to the antenna FEEs and both back-end electronics enclosures by the EFOY automatic power system at the control hub, where the back-end electronics enclosures were also kept. For these measurements, the solar panels were switched off to reduce daytime self-generated RFI from the solar charge controller.

To correlate two sets of autonomous baseband data, they must first be aligned in time. Raw baseband data is saved in chunked files approximately every minute, so a first estimate of the re-

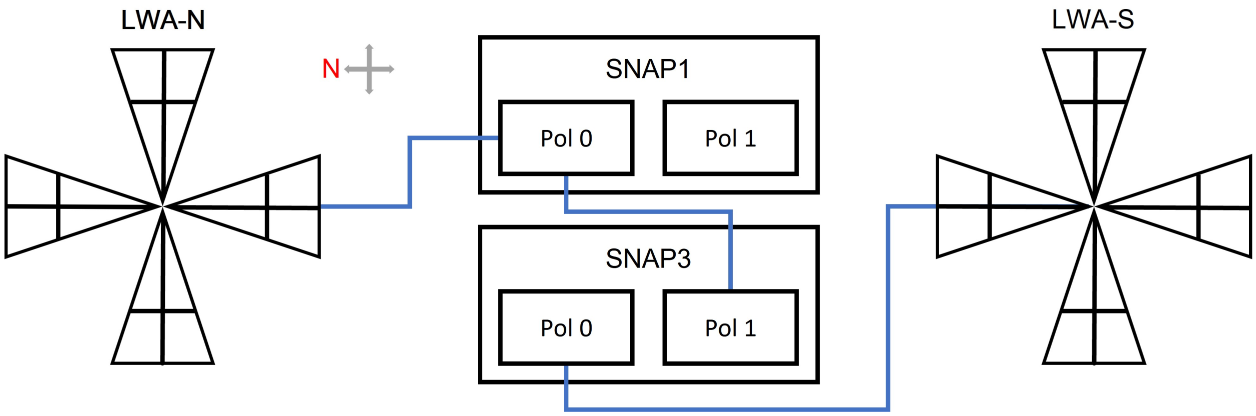

Figure 4.4: Diagram of the two-element autonomous interferometer setup with simultaneous directly-computed cross-spectrum. Blue lines indicate signal paths. The two back-end electronics enclosures (SNAP1 and SNAP3) are, respectively, connected to the north-aligned polarizations of LWA-N and LWA-S. In each case, the output from the antenna is passed to the first input (pol0) on the relevant SNAP board. An additional connection is made which also passes the LWA-N output to the second input (pol1) of SNAP3, whose FPGA directly computes the cross-spectrum between the co-aligned polarizations of LWA-N and LWA-S for verification purposes. Pol1 of SNAP1 is left empty and terminated with $50\,\Omega$.

quired offset between both datasets is obtained by comparing the files' timestamps, which have 1-second precision. Once the two sets of baseband data are aligned within a minute of each other using timestamps, the common signal between two baseband files is cross-correlated and the peak in the cross-correlation determines the exact offset needed for the alignment. Then, the cross-correlation in frequency-space between two autonomous antenna stations is calculated with the appropriate timing offset. The binned magnitude of the computed cross-correlation result is shown in Figure 4.5. The shape of the baseband-based cross-spectrum qualitatively agrees with the shape of the directly-computed cross-spectrum, although the amplitudes of the fringes are different. The difference in fringe amplitude is expected as no corrections has been made for normalization factors relating to the number of samples and the number of bits. Many vertical stripes appear regularly at intervals of $\sim 270\,$kHz intervals and they are likely artifacts from either local or self-generated RFI, potentially from the EFOY methanol fuel cell which exhibited very similar emission behaviour during the manufacturer's electromagnetic interference testing. More work will be required to properly characterize and mitigate self-generated RFI from the hybrid

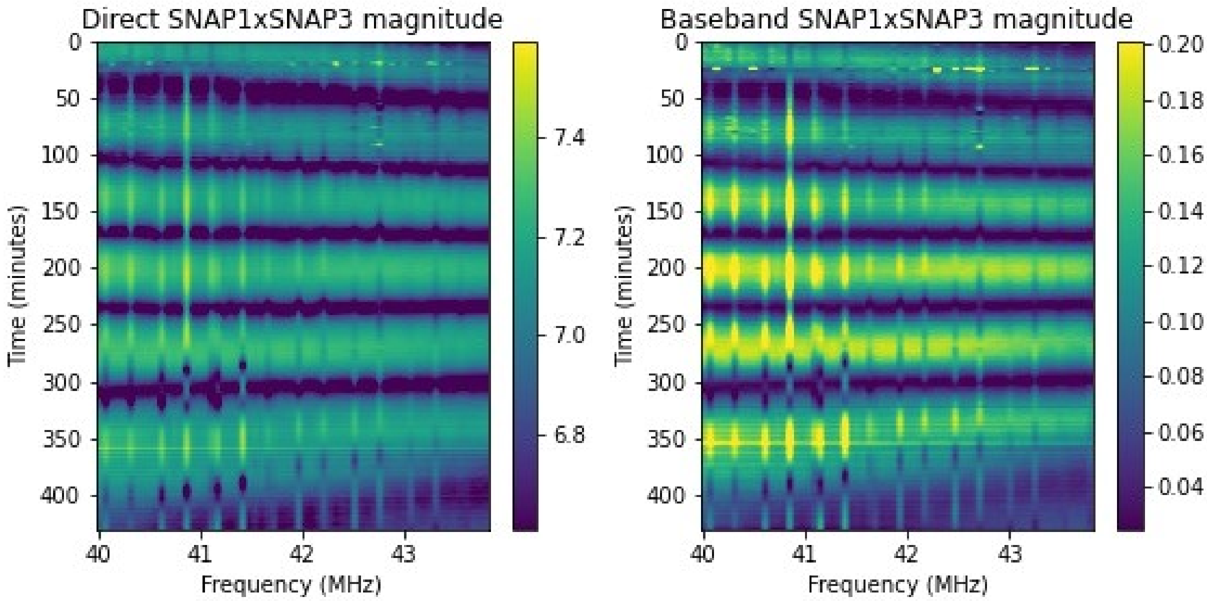

Figure 4.5: Cross-spectrum of co-aligned polarizations from the LWA-N and LWA-S antennas. Each antenna is connected to its own back-end electronics enclosure (SNAP1 and SNAP3, respectively) that independently records 4-bit baseband data between $\sim$ 40–44 MHz. The cross-correlation resulting from the two sets of independent baseband data is shown on the right, while the simultaneous directly-computed cross-spectrum is shown on the left for comparison. The measurements were taken on the night of July 26–27 2021 between 22:12–05:55 local time.

power system. Still, the final configuration of an ALBATROS array will be less sensitive to self-generated RFI than the current batch of short baseline measurements because self-generated RFI is uncorrelated between autonomous stations separated by large baseline distances.

In another test, Figure 4.6 gives the cross-spectrum magnitude for baseband data taken on the night of July 24–25 2021 with the EW-aligned polarizations of the LWA-S and LWA-E antennas. In this cross-spectrum, vertical stripes are noticeably absent, which may mean that the potential source of RFI falls off rapidly with distance since LWA-E is further away from the control hub. Therefore, the vertical stripes may not be problematic in final configuration of an ALBATROS array as autonomous antenna stations are separated by large distances. Unfortunately, a simultaneous directly-computed cross-spectrum was impossible for this measurement because the distance between LWA-E and the LWA-S exceeds the length of our coaxial cables.

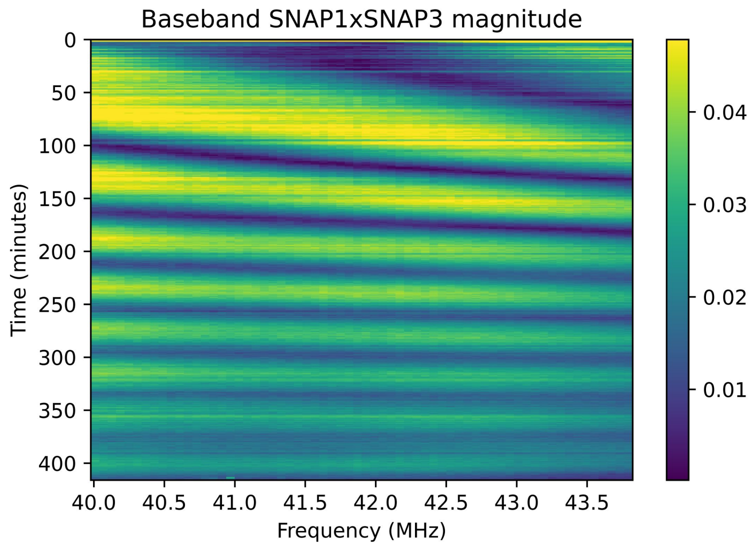

Figure 4.6: Cross-spectrum computed using 4-bit baseband data in the range of $\sim$ 40–44 MHz from co-aligned polarizations of the LWA-S and LWA-E antennas. The baseband was recorded by independent back-end electronics enclosures (SNAP1 and SNAP3) on the night of July 24–25 2021 between 23:58–07:26 local time.

In brief, it has been qualitatively demonstrated that the baseband output of ALBATROS autonomous antennas can be successfully correlated during post-processing of the data. To achieve this goal, several non-trivial additions to the instrument were required. A stable clock is needed to synchronize the ADC sampling rate between individual back-ends, gigabit ethernet is needed for transferring high data rates of baseband data to the RPi, and a hard drive bank with USB multiplexer finally allows large volumes of baseband data to be stored on-site. Further improvements to the alignment between baseband measurements from autonomous antenna stations could be implemented with the help of a simultaneously-recorded window of baseband data centred on the aliased ORBCOMM frequencies.

Chapter 5

Conclusion

In summary, I have explained the cosmological importance for new observations of the redshifted 21-cm signal, especially at low frequencies $\lesssim 30\,\mathrm{MHz}$ corresponding to the cosmic dark ages. The dark ages represent one of the final frontiers in experimental cosmology and hold many more independent modes of information than any other cosmological probe. However, such low frequencies are extremely difficult to observe because of RFI, ionospheric interference, and very strong Galactic foregrounds. Nonetheless, future cosmology experiments will seek to shed light on the cosmic dark ages, both from the ground and from space. ALBATROS will pave the way with modern ground-based high-resolution mapping of the low-frequency radio sky in both hemispheres. ALBATROS arrays will be located at remote radio-quiet sites with favourable ionospheric conditions and will improve upon the resolution of previous low-frequency sky maps using autonomous antenna stations separated by $\sim$ 10-km baseline lengths. The design of the ALBATROS autonomous antenna station was described, including many newly developed systems: mainly a smart EFOY methanol fuel cell and solar hybrid power system from SFC Energy, an updated back-end electronics enclosure, and a brand new MUX enclosure for storing large volumes of baseband data, of which I designed and assembled the two enclosures. Future instrumentation work will focus on characterizing and mitigating self-generated RFI from the new power system. Notably, the solar charge controller will need additional filtering to reduce self-generated RFI during daytime observations, while self-generated RFI from the fuel cell will need to be measured. Work will also continue on designing an optimized antenna and FEE combination for low-frequency observing. In this regard, I outlined a novel method for determining the sky noise dominance of electrically small dipole antennas and op-amp-based FEEs from electromagnetic simulations. Prototype designs of antennas and FEEs have already been built and their low-frequency performance is currently being investigated. Lastly, various options are being examined for the purpose of satellite-based telemetry and status monitoring of the remote antenna stations.

I also produced predictive maps of RFI propagation over large areas which accounted for signal losses due to the topology of the region's terrain. The results suggested that the surroundings of the Manicouagan reservoir would be a good site for ALBATROS testing because of its low RFI levels relative to the local region and its increased accessibility compared to Marion Island and MARS. As such, the first deployment to the Manicouagan reservoir was realized in Summer 2021, during which I performed RFI measurements and installed antennas near Uapishka Station. The first-ever cross-spectrum computed from the baseband data recorded by two independent back-end electronics enclosures was also presented. Two LWA antennas and one back-end electronics enclosure were left running at the end of the deployment, so a large volume of data has potentially been collected over the last few months. The site at Uapishka Station will continue to be used by ALBATROS for long-term engineering runs and robustness tests, especially during the winter months.

On Marion Island, Nivek Ghazi is currently the first dedicated ALBATROS and PRIZM winterover personel, which allows unprecedented access for monitoring and maintenance of the instrument throughout the year. In the near future, new autonomous antenna stations will be installed at predetermined locations around the island. Also, in 2022, ALBATROS crew will likely return to MARS for the first time since 2019 due to travel cancellations during the global pandemic, where more autonomous antenna stations will also be installed.

Bibliography

Bahcall, N. A. 2015, Hubble's Law and the expanding universe, Proceedings of the National Academy of Science, 112, 3173

Barkana, R. 2018, Possible interaction between baryons and dark-matter particles revealed by the first stars, Nature, 555, 71

Baumann, D. 2012, TASI Lectures on Inflation, arXiv e-prints, arXiv:0907.5424

Bentum, M. J., Verma, M. K., Rajan, R. T., et al. 2020, A roadmap towards a space-based radio telescope for ultra-low frequency radio astronomy, Advances in Space Research, 65, 856

Bilitza, D. 2018, IRI the International Standard for the Ionosphere, Advances in Radio Science, 16, 1

Bowman, J. D., Rogers, A. E. E., Monsalve, R. A., Mozdzen, T. J., & Mahesh, N. 2018, An absorption profile centred at 78 megahertz in the sky-averaged spectrum, Nature, 555, 67

Brandenberger, R. H. 2011, Introduction to Early Universe Cosmology, arXiv e-prints, arXiv:1103.2271

Burns, J. O. 2021, Transformative science from the lunar farside: observations of the dark ages and exoplanetary systems at low radio frequencies, Philosophical Transactions of the Royal Society A: Mathematical, Physical and Engineering Sciences, 379, 20190564

Burns, J. O., Hallinan, G., Lux, J., et al. 2019, NASA Probe Study Report: Farside Array for Radio Science Investigations of the Dark ages and Exoplanets (FARSIDE), arXiv e-prints, arXiv:1911.08649

Cane, H. V. 1979, Spectra of the non-thermal radio radiation from the galactic polar regions., Monthly Notices of the Royal Astronomical Society, 189, 465

Cane, H. V., & Whitham, P. S. 1977, Observations of the southern sky at five frequencies in the range 2 - 20 MHz., Monthly Notices of the Royal Astronomical Society, 179, 21

Caswell, J. L. 1976, A map of the northern sky at 10 MHz., Monthly Notices of the Royal Astronomical Society, 177, 601

Chen, X., Burns, J., Koopmans, L., et al. 2019, Discovering the Sky at the Longest Wavelengths with Small Satellite Constellations, arXiv e-prints, arXiv:1907.10853

Chiang, H. C., Dyson, T., Egan, E., et al. 2020, The Array of Long Baseline Antennas for Taking Radio Observations from the Sub-Antarctic, Journal of Astronomical Instrumentation, 9, 2050019

Cohen, A., Fialkov, A., & Barkana, R. 2018, Charting the parameter space of the 21-cm power spectrum, Monthly Notices of the Royal Astronomical Society, 478, 2193

Cong, Y., Yue, B., Xu, Y., et al. 2021, An Ultralong-wavelength Sky Model with Absorption Effect, Astrophysical Journal, 914, 128

de Lera Acedo, E. 2019, REACH: Radio Experiment for the Analysis of Cosmic Hydrogen, in 2019 International Conference on Electromagnetics in Advanced Applications (ICEAA), 0626–0629

Dilullo, C., Taylor, G. B., & Dowell, J. 2020, Using the Long Wavelength Array to Search for Cosmic Dawn, Journal of Astronomical Instrumentation, 9, 2050008

Dowell, J., & Taylor, G. B. 2018, The Radio Background below 100 MHz, Astrophysical Journal Letters, 858, L9

Dyson, T., Chiang, H. C., Egan, E., et al. 2021, Radio-Frequency Interference at the McGill Arctic Research Station, Journal of Astronomical Instrumentation, 10, 2150007

Eastwood, M. W., Anderson, M. M., Monroe, R. M., et al. 2018, The Radio Sky at Meter Wavelengths: m-mode Analysis Imaging with the OVRO-LWA, Astronomical Journal, 156, 32

Ellingson, S. W. 2005, Antennas for the Next Generation of Low-Frequency Radio Telescopes, IEEE Transactions on Antennas and Propagation, 53, 2480

Ellis, G. R. A., & Hamilton, P. A. 1966, Cosmic Radio Noise Survey at 4.7 Mc/s, Astrophysical Journal, 143, 227

Ellis, G. R. A., & Mendillo, M. 1987, A 1.6 MHz survey of the galactic background radio emission., Australian Journal of Physics, 40, 705

Erickson, B. 2003, Integration Times vs. Sky Noise Dominance, LWA Memo #23, http://www.ece.vt.edu/swe/lwa/

Farr, T. G., Rosen, P. A., Caro, E., et al. 2007, The Shuttle Radar Topography Mission, Reviews of Geophysics, 45, RG2004

Field, G. B. 1958, Excitation of the Hydrogen 21-CM Line, Proceedings of the IRE, 46, 240

Fixsen, D. J. 2009, The Temperature of the Cosmic Microwave Background, Astrophysical Journal, 707, 916

Furlanetto, S. R., Oh, S. P., & Briggs, F. H. 2006, Cosmology at low frequencies: The 21 cm transition and the high-redshift Universe, Physics Reports, 433, 181

Hendricksen, I. T. 2021, Development of a Highly Integrated and Power-Efficient Miniature Version of the MIST Analog Chain, Bulletin of the AAS, 53, https://baas.aas.org/pub/2021n1i533p04

Hickish, J., Abdurashidova, Z., Ali, Z., et al. 2016, A Decade of Developing Radio-Astronomy Instrumentation using CASPER Open-Source Technology, Journal of Astronomical Instrumentation, 5, 1641001

Hicks, B. C., Paravastu-Dalal, N., Stewart, K. P., et al. 2012, A Wide-Band, Active Antenna System for Long Wavelength Radio Astronomy, Proceedings of the Astronomical Society of the Pacific, 124, 1090

Hinshaw, G., Weiland, J. L., Hill, R. S., et al. 2009, Five-Year Wilkinson Microwave Anisotropy Probe Observations: Data Processing, Sky Maps, and Basic Results, Astrophysical Journal Supplement Series, 180, 225

Huang, Q.-Z., Wu, F.-Q., Ansari, R., & Chen, X. 2018, Extracting 21 cm signal by frequency and angular filtering, Research in Astronomy and Astrophysics, 18, 114

Hubble, E. 1929, A Relation between Distance and Radial Velocity among Extra-Galactic Nebulae, Proceedings of the National Academy of Science, 15, 168

Hufford, G. A., Longley, A. G., & Kissick, W. A. 1982, A Guide to the Use of the ITS Irregular Terrain Model in the Area Prediction Mode, Tech. rep., NTIA Report 82-100

Jarvis, A., Reuter, H. I., Nelson, A., & Guevara, E. 2007, Hole-filled seamless SRTM data V4, https://srtm.csi.cgiar.org

Jester, S., & Falcke, H. 2009, Science with a lunar low-frequency array: From the dark ages of the Universe to nearby exoplanets, New Astronomy Reviews, 53, 1

Karki, J. 2003, Calculating noise figure in op amps, Tech. rep., Texas Instruments

Kasampalis, S., Lazaridis, P. I., Zaharis, Z. D., et al. 2013, Comparison of Longley-Rice, ITM and ITWOM propagation models for DTV and FM broadcasting, in 2013 16th International Symposium on Wireless Personal Multimedia Communications (WPMC), 1–6

Kasampalis, S., Lazaridis, P. I., Zaharis, Z. D., et al. 2015, Longley-Rice model prediction inaccuracies in the UHF and VHF TV bands in mountainous terrain, in 2015 IEEE International Symposium on Broadband Multimedia Systems and Broadcasting, 1–5

Lazaridis, P., Bizopoulos, A., Kasampalis, S., Cosmas, J., & Zaharis, Z. D. 2013, Evaluation of prediction accuracy for the Longley-Rice model in the FM and TV bands, in XI International Conference–ETAI 2013, 1–4

Line, J. L. B., McKinley, B., Rasti, J., et al. 2018, In situ measurement of MWA primary beam variation using ORBCOMM, Publications of the Astronomical Society of Australia, 35, e045

Liu, A., & Shaw, J. R. 2020, Data Analysis for Precision 21 cm Cosmology, Proceedings of the Astronomical Society of the Pacific, 132, 062001

Loeb, A., & Zaldarriaga, M. 2004, Measuring the Small-Scale Power Spectrum of Cosmic Density Fluctuations through 21cm Tomography Prior to the Epoch of Structure Formation, Physical Review Letters, 92, 211301

Longley, A. G., & Rice, P. L. 1968, Prediction of Tropospheric Radio Transmission Loss Over Irregular Terrain–A Computer Method 1968, Tech. rep., ESSA Tech. Report ERL 79-ITS 67, https://www.its.bldrdoc.gov/publications/download/erl%2079-its%2067.pdf

Mathewson, D. S., Broten, N. W., & Cole, D. J. 1965, A survey of the southern sky at 30 Mc/s, Australian Journal of Physics, 18, 665

Mo, H., van den Bosch, F. C., & White, S. 2010, Galaxy Formation and Evolution

Moso, T. 2021, Low-Frequency Observations of the Radio Sky from Marion Island, Master's thesis, University of Kwa-Zulu Natal

Nambissan T., J., Subrahmanyan, R., Somashekar, R., et al. 2021, SARAS 3 CD/EoR Radiometer: Design and Performance of the Receiver, arXiv e-prints, arXiv:2104.01756

Neben, A. R., Bradley, R. F., Hewitt, J. N., et al. 2015, Measuring phased-array antenna beampatterns with high dynamic range for the Murchison Widefield Array using 137 MHz ORBCOMM satellites, Radio Science, 50, 614

Nhan, B., Bradley, R. F., & Burns, J. O. 2018, The Cosmic Twilight Polarimeter: A Model-Independent Approach to Measure the Sky-averaged Foreground Spectrum for Global 21-cm Cosmology, in American Astronomical Society Meeting Abstracts, Vol. 232, American Astronomical Society Meeting Abstracts #232, 102.04

Novaco, J. C., & Brown, L. W. 1978, Nonthermal galactic emission below 10 megahertz., Astrophysical Journal, 221, 114

Paravastu, N., Hicks, B., Aguilera, E., et al. 2007, Impedance Measurements of the Big Blade and Fork Antennas on Ground Screens at the LWDA Site, LWA Memo #90, http://www.ece.vt.edu/swe/lwa/

Peebles, P. J. E. 1968, Recombination of the Primeval Plasma, Astrophysical Journal, 153, 1

Peterson, J. B. 2021, The High-Z All-Sky Spectrometer, 4th Global 21-cm Workshop, Network for Exploration and Space Science at the University of Colorado Boulder, https://youtu.be/WcPXqomrl3w

Philip, L., Abdurashidova, Z., Chiang, H. C., et al. 2019, Probing Radio Intensity at High-Z from Marion: 2017 Instrument, Journal of Astronomical Instrumentation, 8, 1950004

Planck Collaboration, Aghanim, N., Akrami, Y., et al. 2020, Planck 2018 results. VI. Cosmological parameters, Astronomy and Astrophysics, 641, A6

Platania, P., Bensadoun, M., Bersanelli, M., et al. 1998, A Determination of the Spectral Index of Galactic Synchrotron Emission in the 1-10 GHz Range, Astrophysical Journal, 505, 473

Price, D. C., Greenhill, L. J., Fialkov, A., et al. 2018, Design and characterization of the Large-aperture Experiment to Detect the Dark Age (LEDA) radiometer systems, Monthly Notices of the Royal Astronomical Society, 478, 4193

Pritchard, J. R., & Loeb, A. 2008, Evolution of the 21cm signal throughout cosmic history, Physical Review D, 78, 103511

—. 2010, Cosmology: Hydrogen was not ionized abruptly, Nature, 468, 772

—. 2012, 21 cm cosmology in the 21st century, Reports on Progress in Physics, 75, 086901

Reber, G. 1968, Cosmic static at 144 meters wavelength, Journal of the Franklin Institute, 285, 1

Riess, A. G., Macri, L. M., Hoffmann, S. L., et al. 2016, A 2.4% Determination of the Local Value of the Hubble Constant, Astrophysical Journal, 826, 56

Roger, R. S., Costain, C. H., Landecker, T. L., & Swerdlyk, C. M. 1999, The radio emission from the Galaxy at 22 MHz, Astronomy and Astrophysics Supplements, 137, 7

Roos, M. 2008, Expansion of the Universe - Standard Big Bang Model, arXiv e-prints, arXiv:0802.2005

Ryden, B. 2016, Introduction to Cosmology

Santos, M. G., Ferramacho, L., Silva, M. B., Amblard, A., & Cooray, A. 2010, Fast large volume simulations of the 21-cm signal from the reionization and pre-reionization epochs, Monthly Notices of the Royal Astronomical Society, 406, 2421

Singh, S., Subrahmanyan, R., Udaya Shankar, N., et al. 2018, SARAS 2 Constraints on Global 21 cm Signals from the Epoch of Reionization, Astrophysical Journal, 858, 54

Stutzman, W. L., & Thiele, G. A. 2012, Antenna Theory and Design (John Wiley & Sons)

Wouthuysen, S. A. 1952, On the excitation mechanism of the 21-cm (radio-frequency) interstellar hydrogen emission line., Astronomical Journal, 57, 31

Zakharenko, V., Konovalenko, A., Zarka, P., et al. 2016, Digital Receivers for Low-Frequency Radio Telescopes UTR-2, URAN, GURT, Journal of Astronomical Instrumentation, 5, 1641010

Zaldarriaga, M., Furlanetto, S. R., & Hernquist, L. 2004, 21 Centimeter Fluctuations from Cosmic Gas at High Redshifts, Astrophysical Journal, 608, 622

Zarka, P., Tagger, M., Denis, L., et al. 2015, NenUFAR: Instrument description and science case, in 2015 International Conference on Antenna Theory and Techniques (ICATT), 1–6